Tailoring of interface modes in topologically protected edge states with hourglass lattice metamaterials

Harsh Mirani [a],[1], Vivek Gupta [a],[1], Sondipon Adhikari [b], Bishakh Bhattacharya [a],[*]

[a] *Smart Materials, Structures and Systems Laboratory, Department of Mechanical Engineering, Indian Institute of Technology, Kanpur, 208016, Uttar Pradesh, India*
[b] *James Watt School of Engineering, The University of Glasgow, Glasgow, G12 8QQ, United Kingdom*

ARTICLE INFO

ABSTRACT

Nonreciprocity and topologically protected wave propagation have significant implications on how energy and information are transmitted or guided within materials to control or mitigate its effects. The major challenge in tailoring interface mode arises from challenges related to the customizability and linearity of interface lattice, moreover, there is a scarce of experimental analysis reported in the literature. Our study has focused on obtaining topologically protected nontrivial interface modes at a specific frequency by breaking the inversion symmetry through novel hourglass metastructure both theoretically and experimentally. Detailed work on wave transmission, dispersion, and bandgap analysis are carried out considering topological metamaterials. New cellular configurations based on regular honeycomb and auxetic cells, and variations of their geometric parameters responsible for interface mode tuning are reported here. A generalized theoretical scheme for different combinations of the hourglass lattice is derived at the interface, and consequent energy harvesting and damping prospects are reported. Analytical modeling of topological metamaterial lattice along with numerical simulation, additive layer manufacturing (3D printing), and finally experimental validations are carried out to justify the behavior and reveal the underlying physics responsible for its unique behavior. Three types of configurations including hourglass lattice at the interface define a general framework for introducing lattice-based imperfections in the continuous elastic structure for potential engineering applications. The localized topological interface mode obtained within the bandgap can be tuned significantly with the help of latticed hourglass and may be utilized for the purpose of wave guiding, wave focusing, and energy harvesting within the isolation zone.

1. Introduction

Wave propagation including wave manipulation and waveguiding in engineered microstructures have been extensively pursued by the researchers associated with condensed matter physics [1]. With reference to acoustic, elastic, electromagnetic, and electronic field, topologically protected energy transmission by waves is a well studied phenomenon in physics and engineering [2]. Various fields of applications such as aerospace, acoustics [3,4], electronics [5], photonics [6], mechanics [7], and optomechanics [8] have brought out the characteristics of such wave propagation. Recently, this study has been extended to elastic wave propagation by

Nomenclature

χ	Modified stiffness parameter
γ	Stiffness parameter
μ	Wave number
ν	Poisson's ratio
Ω	Non-dimensional frequency
ω	Natural frequency
ω_r	Natural resonant frequency
τ	Non-dimensional time scale
θ_c	Cell lattice angle
E_s	Modulus of Elasticity of hourglass
H	Height of hourglass metastructure
h	Height of single dome of hourglass
k	Mean stiffness value of spring
k_1	Spring stiffness higher than mean stiffness
k_2	Spring stiffness lower than mean stiffness
l_c	Beam length of regular honeycomb and auxetic cells
m	Mass of unit cell
r	Radius of curvature joining double dome
t	Thickness of hourglass metastructure
t_c	Beam thickness of regular honeycomb and auxetic cells
$u_{c,0}$	Displacement of the cth mass in 0th unit cell
$u_{v,j}$	Displacement of the vth mass in jth unit cell
$u_{w,j}$	Displacement of the wth mass in jth unit cell

metamaterials whose distinctive material properties are due to their structure and geometry, rather than their inherent material property [9–12]. These materials have periodic structures or systems that exhibit spatial periodicity manifested by internal system geometry, material phases, or repeating boundary conditions. The engineering of band structure using metamaterials serves as a unifying subject of research in a vast range of physical domains, including directional propagation, wave focusing [13], acoustic cloaking [14], negative Poisson's ratio [15], negative refraction [16], wave alteration [17], topological edge states [11,18], multistable metamaterials [19] and subwavelength bandgaps [20].

More recently, in this direction a novel class of wave mechanisms known as "topological edge states" [18], has been explored from the mechanical wave propagation perspective. The ability of a wave to travel in a single direction along a surface without back-scattering, regardless of the existence of defects or disorder, is known to be inspired by the electronic edge states occurring in topological insulators, and possess a striking and technologically promising area of research. One of the important properties that can be achieved to understand how information and energy are transmitted using wave-based phenomena is the band topology in topological metamaterials, which results in unique characteristics like localized interface mode within the bandgap [21,22].

Two phononic crystal lattices with different configurations combined with each other would lead to edge state modes within the bandgap [18,23,24]. The present study is based on linking periodic assemblies that are inverted copies of each other and breaking inversion symmetry within a unit cell of a periodic medium. The one-dimensional linear chain incorporated comprises the spring–mass lattice with the stiffness values of the springs alternating about the mean. The interface mass acts as a point of breaking symmetry, and the phenomena of a localized mode within the bandgap are observed [18,25–28]. In order to study the dynamic response, the springs attached adjacent to the interface mass are replaced with the hourglass metastructures [29–31] of different classes namely auxetic and honeycomb, and integrated into the system. The hourglass metastructure behaves as a spring in the linear chain, as it has been observed that the equivalent stiffness of the hourglass metastructure can be assumed to be linear within a small deflection range. It is required to create an ideally dome-shaped structures, popularly known as synclastic shapes [32], using these auxetic structures [33–35] with negative Poisson's ratios. On a large scale, it is presumable that the honeycomb is a continuous part or sample made up of a sufficient number of periodic unit cells, enabling homogeneity of its overall mechanical properties. In order to analyze the system as a whole, periodic boundary conditions were applied using the Bloch wave formulation [36,37]. The band diagrams contain information on bandgaps, frequency, and interface modes that have been obtained by applying Floquet–Bloch periodic boundary conditions with the consideration of topological effects [37–39]. Recently advancements have been made in the realization of interface modes in topological lattices using beams with periodically varying structures [18,26,40] and symmetry-breaking principles, where the idea of alternating spring stiffness is created by periodically changing the cross-section of beam [41,41]. Topological metamaterials provide an exciting pathway towards materials with robust functionalities [42]. Origami and Kirigami, have recently emerged as prototypical routes for the design of mechanical metamaterials due to their characteristics such as easy fabrication and folding patterns, bistability, and self-assembly ability [43]. Moreover, the
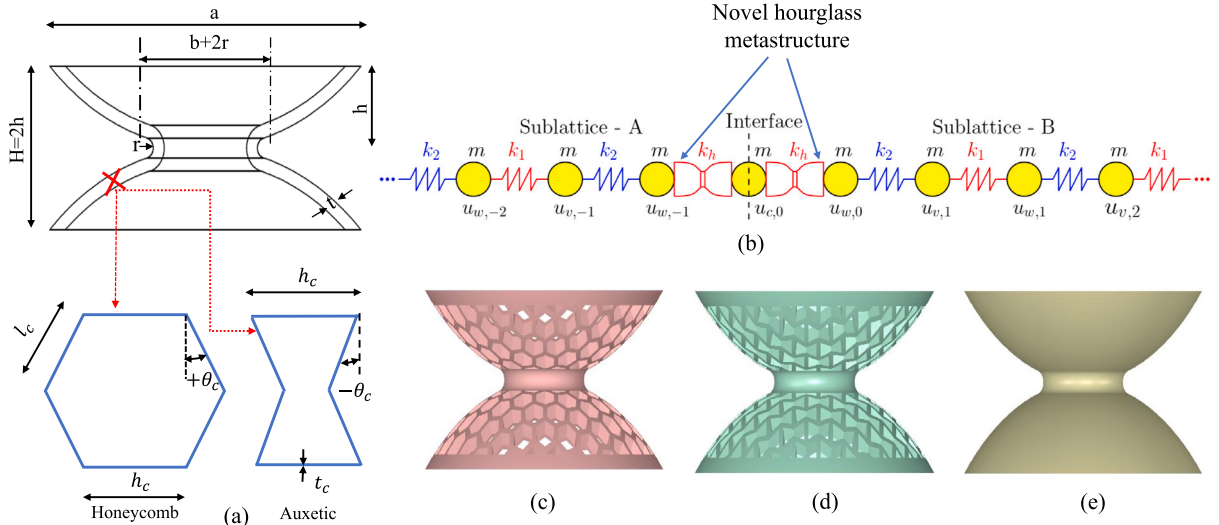
Fig. 1. (a) Details of geometric specifications of hourglass lattice metastructure along with the honeycomb and auxetic cellular configurations and their dimensions. (b) Schematic representation of a novel 1D periodic spring–mass system with the introduction of hourglass metastructure at the interface junction to break the inversion symmetry. (c, d, e) Representation of homogeneous type hourglass lattice metastructure with the honeycomb, auxetic and solid shell configurations.

effect of material damping on the topological interface states and energy localization performance is analyzed and it is found that at high frequencies, the damping could play a vital role in the strength of the interface state [44,45]. Very little literature has been reported on the application of such metastructures as the customizable interface lattice in topological metamaterials. The challenges to achieving singularity at its precise interface location pose major challenges to implementing it practically. We demonstrated experimentally and validated the claims made in this report so far. However, the experimental demonstration of interface mode using spring–mass based one-dimensional lattice and the tuning of the same by inserting hourglass metastructure is currently reported in this study. Further, the piezoelectric transduction is used for transforming vibrational energy into electrical energy such that the proposed system can also be used for energy harvesting [46].

The primary goal of this research is to create interface modes in topological metamaterial lattices with the aid of metastructures, which results in a novel idea for obtaining high amplitude response within the bandgap that may be used for wave focusing at particular frequencies. With the integration of tunable metastructure, we successfully achieve our main objective of realizing interface modes in topological metamaterial lattice. Experimental validations were conducted using Laser Doppler Vibrometer (LDV) to analyze the complete dynamics and wave propagation behavior. Additionally, we have demonstrated the idea of energy harvesting within the bandgap at specific frequencies, which has promising applications in the areas of wave tuning, and energy harvesting. The interdependency of hourglass stiffness with its constitutive cell angle has been utilized to tune the interface modes, which has good potential for energy harvesting. This is a new idea for energy harvesting inside the bandgap that has not been reported in the literature.

2. Mathematical modeling

The existence of interface modes in topological metamaterial can be exemplified with an one-dimensional diatomic spring mass lattice chain (shown in Fig. 1) which comprises two sublattices joined through an interface, namely the sublattice - A and sublattice - B. The sublattice chains are made up of diatomic unit cells comprising of identical masses m and alternating springs having stiffnesses k_1 and k_2 respectively. Arrangement of the entire topological lattice is such that at both the sides of the interface mass, stiffness of the spring attached on adjacent sides is the same i.e. either k_1 or k_2. The novel hourglass metastructure [30] possessing stiffness k_h is inserted at the adjacent sides of the interface mass keeping rest of the lattice intact as shown in Fig. 1. The sublattices mounted on adjacent sides of the interface mass are inverted copies (mirror images) of each other which results in topological polarization, achieved by breaking symmetry.

The governing equations of motion under free vibration for a unit cell j on sublattice - A of topological metamaterial can be obtained as,

$$m\ddot{u}_{v,j} + k_2(u_{v,j} - u_{w,j}) + k_1(u_{v,j} - u_{w,j-1}) = 0 \tag{1}$$

$$m\ddot{u}_{w,j} + k_2(u_{w,j} - u_{v,j}) + k_1(u_{w,j} - u_{v,j+1}) = 0 \tag{2}$$

Similarly, the governing equations of motion for a unit cell j on sublattice - B of topological metamaterial can be obtained as,

$$m\ddot{u}_{v,j} + k_1(u_{v,j} - u_{w,j}) + k_2(u_{v,j} - u_{w,j-1}) = 0 \tag{3}$$

$$m\ddot{u}_{w,j} + k_1(u_{w,j} - u_{v,j}) + k_2(u_{w,j} - u_{v,j+1}) = 0 \tag{4}$$

The governing equations of motion for the interface mass (interface unit cell consisting of two masses having displacements $u_{c,0}$ and $u_{w,0}$) are given by,

$$m\ddot{u}_{c,0} + k_h(u_{c,0} - u_{w,-1}) + k_h(u_{c,0} - u_{w,0}) = 0 \tag{5}$$

$$m\ddot{u}_{c,0} + k_h(2u_{c,0} - u_{w,-1} - u_{w,0}) = 0 \tag{6}$$

$$m\ddot{u}_{w,0} + k_h(u_{w,0} - u_{c,0}) + k_2(u_{w,0} - u_{v,1}) = 0 \tag{7}$$

For expressing the above derived governing equations into the non-dimensional form, a non-dimensional time scale $\tau = \left(\sqrt{\dfrac{k}{m}}\right)\tilde{t}$ is incorporated, where $\tilde{t}$ is time.

2.1. Relating γ parameter with the stiffness of auxetic and honeycomb hourglass lattice

Given that the stiffness corresponding to the regular honeycomb hourglass lattice is denoted as k_h and stiffness corresponding to the auxetic hourglass lattice is denoted as k_a, we incorporate these lattices in the arrangement as shown in Fig. 1(b) having k_h at the adjacent side of interface mass and rest of the lattice comprising of linear springs with stiffness k_1 and k_2 respectively. A similar arrangement can also be made for auxetic hourglass metastructures configuration having stiffness k_a at the adjacent sides of the interface mass. Considering,

$$k_1 = k(1 + \gamma) \text{ and } k_2 = k(1 - \gamma) \tag{8}$$

In order to introduce tunability of the stiffnesses that depend on the geometrical parameters of the hourglass, we take k_1 (which represents higher stiffness) as stiffness of regular honeycomb k_h and k_2 (which represents lower stiffness) as stiffness of auxetic hourglass k_a. The linear stiffness is approximated for small deflections of the hourglass lattice [30] which implies,

$$k_h = k(1 + \gamma) \text{ and } k_a = k(1 - \gamma) \tag{9}$$

On comparing the value of γ from Eq. (9), we further obtain

$$\gamma = \left(\frac{k_h}{k} - 1\right) = \left(1 - \frac{k_2}{k}\right) \tag{10}$$

$$\gamma = \frac{k_h - k_2}{k_h + k_2} \tag{11}$$

Eq. (11) shows that the γ parameter is dependent on the stiffness of hourglass metastructure k_h and thereby reflects its dependency on the cell lattice angle θ_c present on the dome shape of the hourglass metastructure.

$$\gamma = f\left(k_h\right) = f\left(\theta_c\right)$$

By using the load–deflection relationship available related to the dome-shaped hourglass metastructure with lattice on its dome from our previously published results [30], the final expression for the external load P and moment M_R generated corresponding to the deflection of a single dome of hourglass metastructure is given by

$$P = \left(\frac{t_c}{l_c}\right)^3 \frac{E_s}{\cos\theta_c \sin\theta_c} \frac{\delta}{(1 - v^2)Ma^3}\left[(h - \delta)(h - \frac{\delta}{2})t + t^3\right] \tag{12}$$

Representing the load–deflection relationship from Eq. (12) as a simplified cubic polynomial having K_1, K_2 and K_3 as controlling parameters of nonlinear stiffness in terms of δ, one can express

$$P = K_1\delta + K_2\delta^2 + K_3\delta^3 \tag{13}$$

where,

$$K_1 = (C_1\, t\, h^2 + C_1\, t^3), K_2 = -\left(\frac{3}{2}\, h\, t\, C_1\right), K_3 = \left(\frac{1}{2}\, t\, C_1\right)$$

$$C_1 = \left(\frac{t_c}{l_c}\right)^3 \frac{E_s \cos\theta_c}{\left(\frac{h_c}{l_c} + \sin\theta_c\right)(\sin\theta_c)^2} \frac{1}{(1 - v^2)Ma^2}$$

$$\frac{1}{M} = \left[\frac{r + 1}{r - 1} - \frac{2}{\log r}\right]\pi\left(\frac{r}{r - 1}\right)^2, \quad \text{where } r = \frac{a}{b}$$

To obtain the relation of load–deflection, assuming it as a combination of two nonlinear springs in series with spring constants C_1 and C_2 resulting in satisfying the force characteristics $P_1 = C_1x^N$ and $P_2 = C_2y^N$ which after expressing them as $z = x + y$ lead to the following expression as obtained in [30], and reported here for completeness.

For odd power of N; $N = 2n + 1$

$$P = \frac{1}{\left(\left(\frac{1}{C_1}\right)^{\frac{1}{2n+1}} + \left(\frac{1}{C_2}\right)^{\frac{1}{2n+1}}\right)^{2n+1}} Z^{2n+1} \tag{14}$$

For even power of N; $N = 2n$

$$P = \frac{1}{\left(\left(\frac{1}{C_1}\right)^{\frac{1}{2n}} + \left(\frac{1}{C_2}\right)^{\frac{1}{2n}}\right)^{2n}} Z^{2n} \tag{15}$$

Considering the hourglass metastructure as the series combination of two identical nonlinear springs expressed by Eq. (13) upon incorporating Eqs. (14) and (15), yields the expression of equivalent load P_{eq} for homogeneous configuration as

$$P_{eq} = \frac{K_1}{2}\delta_{eq} + \frac{K_2}{4}\delta_{eq}^2 + \frac{K_3}{8}\delta_{eq}^3 \tag{16}$$

The experimental results and load–deflection plot mentioned in [30] take into consideration only the linear relation between load and deflection since in the small deflection range, it shows a linear relationship. Finally, relating the stiffness k_h to lattice cell angle θ_c i.e., $k_h = f(\theta_c)$, we can relate the dependency of γ to θ_c as $\gamma = f(\theta_c)$.

In order to obtain the dispersion relationship using Bloch formulations, an infinite periodic diatomic lattice having identical masses and alternating spring stiffness as k_1 and k_2 is considered without the presence of interface mass which earlier acted as a point of breaking symmetry [47]. Let the governing equation of the unit cell j of the diatomic periodic lattice be given as,

$$m\ddot{u}_{v,j} + k_1(u_{v,j} - u_{w,j}) + k_2(u_{v,j} - u_{w,j-1}) = 0 \tag{17}$$

$$m\ddot{u}_{w,j} + k_1(u_{w,j} - u_{v,j}) + k_2(u_{w,j} - u_{v,j+1}) = 0 \tag{18}$$

Substituting the value of $k_1 = k(1 + \gamma)$ and $k_2 = k(1 - \gamma)$ in Eqs. (17) and (18) results in the non-dimensional form as:

$$\ddot{u}_{v,j} + 2u_{v,j} - (1 + \gamma)u_{w,j} - (1 - \gamma)u_{w,j-1} = 0 \tag{19}$$

$$\ddot{u}_{w,j} + 2u_{w,j} - (1 + \gamma)u_{v,j} - (1 - \gamma)u_{v,j+1} = 0 \tag{20}$$

The plane wave solution of the form $u_j = (u_{v,j}, u_{w,j}) = A(\mu)e^{i(\Omega\tau+\mu j)}$ is implemented in Eqs. (19) and (20) which results in the eigen value problem of Eq. (21), where Ω is used to represent frequency, $i = \sqrt{-1}$ is imaginary number and μ is non-dimensional wave number.

$$\begin{pmatrix} 2 - \Omega^2 & -(1+\gamma) - (1-\gamma)e^{-i\mu} \\ -(1+\gamma) - (1-\gamma)e^{i\mu} & 2 - \Omega^2 \end{pmatrix} \begin{pmatrix} A_v \\ A_w \end{pmatrix} = \Omega^2 \begin{pmatrix} A_v \\ A_w \end{pmatrix} \tag{21}$$

Taking into account wavenumber along the first Irreducible Brillouin zone (IBZ) i.e. $\mu \in [0, \pi]$ and evaluating the expression leads to dispersion relation Ω depending upon μ and γ.

$$\Omega = \sqrt{2 \pm \sqrt{2 + 2\gamma^2 + 2(1 - \gamma^2)\cos\mu}} \tag{22}$$

The two solutions correspond to optical branch $\Omega_1 = \sqrt{2 + \sqrt{2 + 2\gamma^2 + 2(1 - \gamma^2)\cos\mu}}$ and acoustic branch $\Omega_2 = \sqrt{2 - \sqrt{2 + 2\gamma^2 + 2(1 - \gamma^2)\cos\mu}}$ can be utilized to obtain the plots of the dispersion relation for varying values of γ as represented in Fig. 2. For $\gamma = 0$, the bandgap is zero leading to the acoustic and optical branch meeting each other when evaluated at $\mu = \pi$. While for $\gamma \neq 0$ the non-dimensional parametric width of the bandgap is given by

$$\Omega \in \left(\sqrt{2(1 - |\gamma|)}, \sqrt{2(1 + |\gamma|)}\right) \tag{23}$$

The eigenvector corresponding to the optical and acoustic branch can be obtained respectively as $\left[\begin{array}{c} -\dfrac{(\gamma + 1)e^{-i\mu} - \gamma + 1}{\sqrt{2 - 2\gamma^2\cos\mu + 2\gamma^2 + 2\cos\mu}} \\ 1 \end{array}\right]$

and $\left[\begin{array}{c} \dfrac{(\gamma + 1)e^{-i\mu} - \gamma + 1}{\sqrt{2 - 2\gamma^2\cos\mu + 2\gamma^2 + 2\cos\mu}} \\ 1 \end{array}\right]$. Also evaluating them at $\mu = \pi$, we obtain the eigenvector corresponding to the frequency of symmetric mode which is given by $\begin{pmatrix} A_v \\ A_w \end{pmatrix} = \dfrac{1}{\sqrt{2}}\begin{pmatrix} 1 \\ 1 \end{pmatrix}$ while the eigenvector corresponding to the frequency of anti-symmetric mode is given by $\begin{pmatrix} A_v \\ A_w \end{pmatrix} = \dfrac{1}{\sqrt{2}}\begin{pmatrix} 1 \\ -1 \end{pmatrix}$.
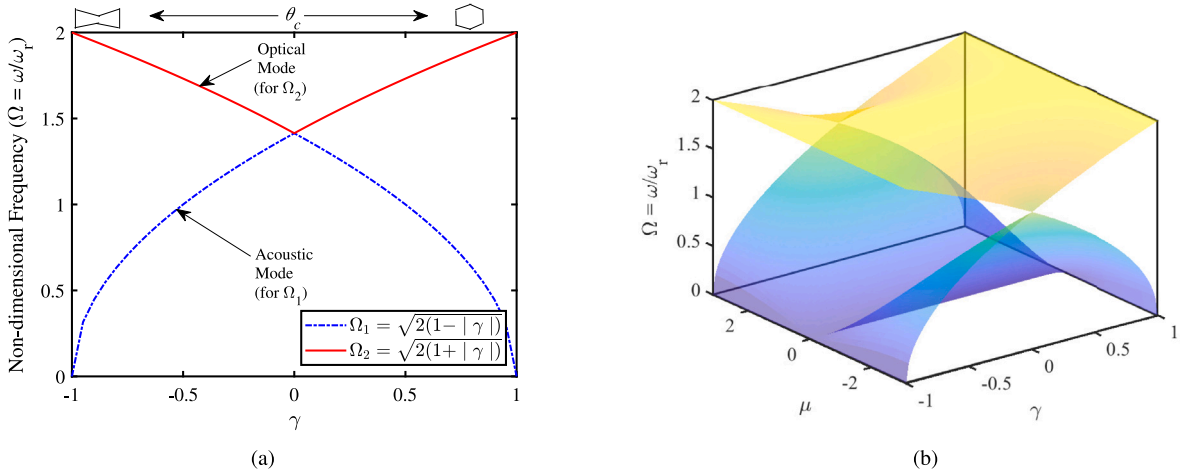
Fig. 2. (a) Acoustic and optical mode frequency variation with the γ parameter along with proportional variation of included angle θ_c (ranging from auxetic to honeycomb cell). The value of $\mu = \pi$ and showing interdependence on lattice of different hourglass metastructures (b) Variation of non-dimensional frequency Ω for optical and acoustic mode with respect to varying values of γ and wave number μ.

The anti-symmetric vector will correspond to a higher frequency from Eq. (23) as the value of γ changes from negative to positive due to band inversion represented in Fig. 2. The localized modes are obtained at the interface of lattices where symmetry breaking happens i.e. $\gamma < 0$ and $\gamma > 0$ in case of hourglass mounted at adjacent sides of the interface mass. The cell lattice angle (θ_c) of the hourglass metastructure can be related to the stiffness parameter γ of the lattice as mentioned in the same section earlier where the value of γ varies from -1 to 1.

2.2. Analytical computation of interface modes

It is known that a non-trivial localized mode is obtained when the two periodic lattices having different Zak phases [48–50] are attached in such a way that one lattice is a mirror copy of another and the point of symmetry breaking assists in obtaining the non-trivial localized mode within the bandgap. The frequency at which the localized mode is observed at the interface in a linear chain can be calculated and the corresponding mode shapes can be derived explicitly. For the purpose of studying the harmonic response of the topological lattice with symmetry broken at the interface, we would consider a finite lattice upon having a considerably large number of unit cells on either side of the interface mass, which would result in the boundary effects being negligible. The unit cells are numbered by parameter j ranging from $j = -N$ to N, while the position of the interface mass is defined at $j = 0$. A harmonic solution of the form $u_j(t) = u_j e^{i\Omega\tau}$ is imposed in the bandgap frequencies to understand the lattice dynamics. The interval of the bandgap frequency may be expressed as

$$\Omega \in \left[\sqrt{2(1-|\gamma|)}, \sqrt{2(1+|\gamma|)} \right] \tag{24}$$

$$\text{or} \quad \Omega > 2 \tag{25}$$

For the implementation of the harmonic solution to the interface mass, we would relate the displacements of adjacent neighboring unit cells $j-1$ and j on any side of the interface mass either left or right. The masses attached to the interface mass $m_{c,0}$ are $m_{w,j-1}$ and $m_{w,j}$ on the left side and right side sublattices respectively. To relate how the displacements of the diatomic atoms of two different unit cells vary as we move from center to right side or left side, we would write the governing equations of the masses of two adjacent unit cells $j-1$ and j. The governing equations of the two masses $m_{w,j-1}$ and $m_{v,j}$ where $j > 0$ (since we are considering the unit cells on the right-hand side of the interface mass $m_{c,0}$) are as follows :

$$m\ddot{u}_{v,j} + k_1(u_{v,j} - u_{w,j}) + k_2(u_{v,j} - u_{w,j-1}) = 0 \tag{26}$$

$$m\ddot{u}_{w,j-1} + k_2(u_{w,j-1} - u_{v,j}) + k_1(u_{w,j-1} - u_{v,j-1}) = 0 \tag{27}$$

The non-dimensional form of Eqs. (26) and (27) would result in

$$(2 - \Omega^2)u_{v,j} - (1+\gamma)u_{w,j} - (1-\gamma)u_{w,j-1} = 0 \tag{28}$$

$$(2 - \Omega^2)u_{w,j-1} - (1-\gamma)u_{v,j} - (1+\gamma)u_{v,j-1} = 0 \tag{29}$$

The relationship between displacements of two adjacent unit cells on the right side of the interface mass would be revealed after rearranging the terms of Eqs. (28) and (29). On the left side of the interface mass, a similar procedure can be used to determine the relationships between neighboring unit cells.

$$
\begin{pmatrix} u_v \\ u_w \end{pmatrix}_j = \begin{pmatrix} \dfrac{\gamma+1}{\gamma-1} & \dfrac{2-\Omega^2}{1-\gamma} \\[2ex] -\dfrac{2-\Omega^2}{1-\gamma} & \dfrac{(2-\Omega^2)^2-(\gamma-1)^2}{1-\gamma^2} \end{pmatrix} \begin{pmatrix} u_v \\ u_w \end{pmatrix}_{j-1} = T \begin{pmatrix} u_v \\ u_w \end{pmatrix}_{j-1}
\tag{30}
$$

where the notation T is used to denote the Transfer matrix which relates displacement of masses in the two adjacent unit cells. Similarly, we can also relate displacement of masses of interface unit cell and the Nth unit cell using the Transfer Matrix method

$$
u_N = T^N u_0
\tag{31}
$$

where $u_0 = \begin{pmatrix} u_{c,0} \\ u_{w,0} \end{pmatrix}^T$ and $u_N = \begin{pmatrix} u_{v,N} \\ u_{w,N} \end{pmatrix}^T$ are the vector components corresponding to the displacements of masses of the interface unit cell and the Nth unit cell respectively. The relation obtained in Eq. (31) depicts that as we move away from the interface unit cell to either left or right the displacements of the unit cells decay exponentially with a power of transfer matrix [10]. Solution of frequency is obtained when the eigenvectors found from the transfer matrix of the considered lattice would satisfy the decay condition. In the bandgap frequency, the eigenvector of T found corresponding to the eigenvalues which are less than 1 are

$$
e = \begin{pmatrix} 2(\Omega^2-2)(1+\gamma) \\ (\Omega^2-2)^2+4\gamma+\Omega\sqrt{(\Omega^2-4)((\Omega^2-2)^2-4\gamma^2)} \end{pmatrix}
\tag{32}
$$

The interface mass governing equation can be written as

$$
2\left(1-\frac{\Omega^2}{2(1+\gamma)}u_{c,0}\right) = (u_{w,0}+u_{w,-1})
\tag{33}
$$

Although the sublattice at the adjacent sides of the interface mass is symmetric and there is a presence of a non-propagating localized mode, the conditions being symmetric about the interface mass would lead to equal displacement movement for the masses which are positioned adjacent to the interface mass

$$
|u_{w,0}| = |u_{w,-1}|
\tag{34}
$$

Implementing the wave solution to the above condition, we may write as $u_{w,-1} = e^{2i\theta}u_{w,0}$ and form the governing equation in the vector form as

$$
u_0 = \begin{pmatrix} u_{c,0} \\ u_{w,0} \end{pmatrix} = \begin{pmatrix} e^{i\theta}\cos\theta \\ 1-\dfrac{\Omega^2}{2(1+\gamma)} \end{pmatrix}
\tag{35}
$$

The decay condition as mentioned in Eq. (31) can be satisfied and we can have u_0 as a non-trivial solution if and only if u is in the subspace which is spanned by $\bar{e}$ eigenvector having eigenvalue less than 1, i.e. $\bar{e} = su_0$ where s is considered as a scalar value. Now comparing the two eigenvectors as u_0 and $\bar{e}$ i.e. Eqs. (32) and (35); equating them with each other would lead to the explicit expressions for the frequencies at which the localized modes are obtained.

$$
\bar{e} = u_0
\tag{36}
$$

$$
\bar{e} = \begin{bmatrix} \overline{e_1} \\ \overline{e_2} \end{bmatrix} = \begin{bmatrix} u_{c,0} \\ u_{w,0} \end{bmatrix}
\tag{37}
$$

This would lead to the computation of the two eigen vectors as

$$
\begin{bmatrix} 2(\Omega^2-2)(1+\gamma) \\ (\Omega^2-2)^2-4\gamma+\Omega\sqrt{(\Omega^2-4)((\Omega^2-2)^2-4\gamma^2)} \end{bmatrix} = \begin{bmatrix} e^{i\theta}\cos\theta \\ 1-\dfrac{\Omega^2}{2(1+\gamma)} \end{bmatrix}
\tag{38}
$$

Upon further solving, the expressions would lead to an equation whose root values of Ω would give the frequency of the localized mode. The component $u_{c,0}$ of the eigenvector u_0 which is the corresponding mode shape for the interface unit cell comprising the two masses is given by $e^{i\theta}\cos\theta$. Hence, the component $u_{c,0} = e^{i\theta}\cos\theta$ can take the value as either 0 or 1 due to the condition of the eigen vector $\bar{e}$ being a scalar multiple of the interface unit cell mode shape u_0 leading to

$$
\frac{\overline{e_1}}{u_{c,0}} = \frac{\overline{e_2}}{u_{w,0}} = c
\tag{39}
$$

$$
2(\Omega^2-2)(1+\gamma)\left(1-\frac{\Omega^2}{2(1+\gamma)}\right) = (\Omega^2-2)^2-4\gamma+\Omega\sqrt{(\Omega^2-4)((\Omega^2-2)^2-4\gamma^2)}e^{i\theta}\cos\theta
\tag{40}
$$

Substituting the value of $\theta = \pi/2$ in Eq. (40) would lead to the expression of following condition $u_{w,-1} = -u_{w,0}$ which can be further expressed as $|u_{w,-1}| = |u_{w,0}|$ and $u_{c,0} = 0$; that makes the interface unit cell mode shape as symmetric.

$$
2(\Omega^2-2)(1+\gamma)\left(1-\frac{\Omega^2}{2(1+\gamma)}\right) = 0
\tag{41}
$$

Hence,

$$(\Omega^2 - 2\gamma - 2)(\Omega^2 - 2) = 0 \tag{42}$$

where non-zero value of γ would result in the value of Ω as

$$\Omega = \sqrt{2} \tag{43}$$

While substituting the value of $\theta = 0$ in Eq. (40) would lead to the condition $u_{w,0} = u_{w,-1}$, and by observing the expression of the transfer matrix and eigenvector one can understand that the mode shape is antisymmetric with respect to the interface mass.

$$2(\Omega^2 - 2)(1 + \gamma)\left(1 - \frac{\Omega^2}{2(1 + \gamma)}\right) = (\Omega^2 - 2)^2 - 4\gamma + \Omega\sqrt{(\Omega^2 - 4)((\Omega^2 - 2)^2 - 4\gamma^2)} \tag{44}$$

Solving Eq. (44), the roots of the equation may be obtained as

$\Omega = \sqrt{2}$; which is symmetric and within the bandgap between acoustic and optical mode

$\Omega = \sqrt{3 + \sqrt{1 + 8\gamma^2}}$; which is antisymmetric and above the optical mode

$\Omega = \sqrt{3 - \sqrt{1 + 8\gamma^2}}$; which is antisymmetric and within the bandgap between acoustic and optical mode

Fig. 3(a) and (b) shows the occurrence of localized interface mode for topological lattice with regular honeycomb hourglass metastructure incorporated; while, Fig. 3(c) and (d) corresponds to auxetic hourglass configuration mounted at adjacent side of the interface. The first and second interface mode frequencies are related to symmetric and antisymmetric mode respectively corresponding to $\gamma > 0$ in the expression $k_h = k_1 = k(1 + \gamma)$ and $k_a = k_2 = k(1 - \gamma)$ following the arrangement at adjacent side of interface mass shown in Fig. 1(b). This represents the case of hard-hard spring mass topological arrangement about the interface mass $(k_1 - k_1)$ that is depicted in Fig. 4(a). The third interface mode frequency which is antisymmetric is obtained when the value of $\gamma < 0$. It can be interpreted that it represents the case of soft-soft spring mass topological arrangement $(k_2 - k_2)$ about the interface mass where the interface mass is having the highest amplitude and the masses adjacent to the interface mass have an amplitude of equal magnitude as depicted in Fig. 4(b). The second and the third frequency of the localized modes obtained are related to the antisymmetric mode which indicates that the unit cells on both sides of the interface move in phase with zero phase difference; while the first frequency mode is associated with the symmetric mode which implies unit cell on adjacent sides of the interface mass move relative to each other with a phase difference of π. From Fig. 4(a) it can be observed that the alternate mass particles are immobile since their normalized displacement is zero causing the remaining mass particles to oscillate about their equilibrium positions. In the symmetric mode, the displacement of the interface mass is equal to zero while the adjacent masses oscillate about their mean position but are in opposite phase. Fig. 4(b) depicts that the absolute displacements at any jth position in the spring–mass lattice system having a topological arrangement with lower stiffness springs at the adjacent sides of the interface mass can be easily obtained using the symmetric condition about the central interface mass. This is because the central interface mode would be non-propagating and similar sub-lattice are attached at their adjacent sides. Hence, for the antisymmetric mode, the displacement of the interface mass is non-zero. The displacement of adjacent masses are equal and in phase. Due to this reason, for the response of $k_1 - k_1$ arrangement at the interface, we measure the response at the mass adjacent to the interface. Contrary to this, in the case of the $k_2 - k_2$ arrangement, the response is measured at the interface mass. The normalized amplitude diagram as shown in Fig. 4(a) and (b) assist in understanding the reason for measurement of response at those specific masses i.e. one on the interface while the other on the mass adjacent to the interface for different cases.

The frequency response of the lattice can be found by considering a finite lattice, however, the length must be large enough so that the boundary effects are negligible. Considering a topological metamaterial lattice consisting of 122 masses having diatomic masses and alternating stiffness spring in one unit cell results in 61 unit cells out of which there is one interface unit cell at the center and 30 unit cells on the left side and 30 on the right side respectively. The value of stiffness parameter γ is considered as 0.4 for numerical computation and the system is given a forced harmonic excitation at one end keeping the other end of the system free. The dynamics of the complete lattice is governed by the following equation

$$\tilde{M}\ddot{u}(\tau) + \tilde{K}u(\tau) = f(\tau) \tag{45}$$

where the lattice is subjected to an externally applied harmonic force $f\cos(\Omega\tau)$. Assuming the solution of the form $u(\tau) = ue^{i\Omega\tau}$, we can reduce the equation to the following form as,

$$\left(\tilde{K} - \Omega^2\tilde{M}\right)u = f \tag{46}$$

Eq. (46) can be transformed into eigenvalue problem by taking $f = 0$ and can be used to find out the eigen frequencies of the chain, such that

$$\left(\tilde{K} - \Omega^2\tilde{M}\right)u = 0 \tag{47}$$

The band gap is obtained for the diatomic periodic chain of spring mass. Converse to this, a localized mode is obtained at the interface mass within the bandgap when the symmetry of the periodic lattice is broken in such a way that the left side sub-lattice and right side sub-lattice of interface mass are mirror replica of each other, as shown in Fig. 3. Acoustic and optical modes are observed and in between them an interface mode at frequency $\Omega = \sqrt{2}$ is observed in the bandgap frequency when the stiffness parameter $\gamma > 0$. Another interface mode is obtained above the optical mode at frequency $\Omega = \sqrt{3 + \sqrt{1 + 8\gamma^2}}$ for the same configuration. Considering
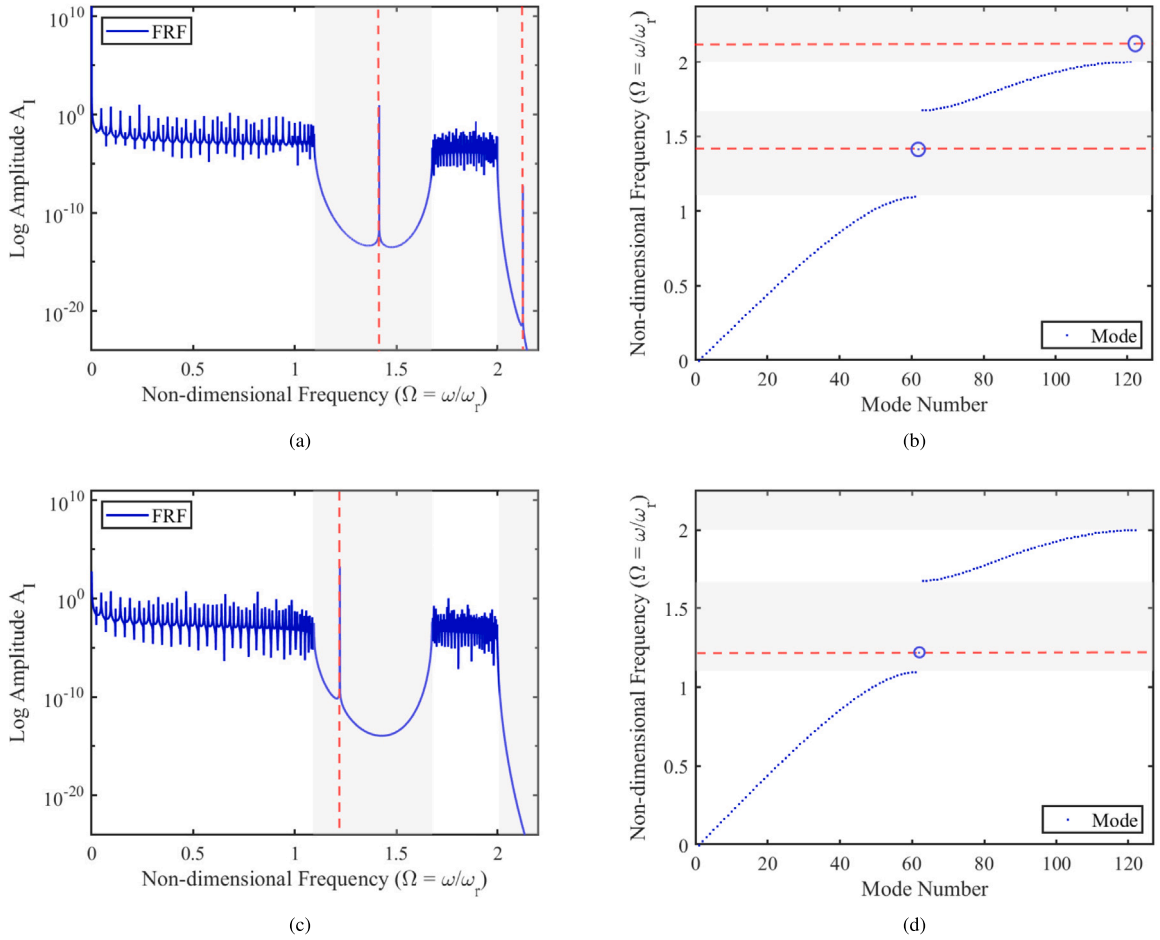
Fig. 3. (a) Frequency response function plot for a 1D topological metamaterial spring–mass lattice with the regular honeycomb hourglass metastructure attached to the opposite sides of the interface mass: identical masses m, $k_1 = k(1 + \gamma)$, and $k_2 = k(1 - \gamma)$, $\gamma = 0.4$. In the central region of the bandgap, a localized interface mode is seen at the interface mass. (b) Natural frequencies of the finite 1D topologically arranged mechanical metamaterial spring–mass lattice comprising 122 masses with regular honeycomb hourglass metastructure k_h attached at both the adjacent sides of the interface mass exhibiting resonating and interface modes over the range of non-dimensional frequencies. (c) Frequency response function plot for 1D topological metamaterial spring–mass lattice : identical masses m, $k_1 = k(1 + \gamma)$ and $k_2 = k(1 - \gamma)$, $\gamma = -0.4$ with auxetic re-entrant angle hourglass metastructure attached at the adjacent sides of the interface mass. A localized interface mode is observed at the interface mass within the bandgap from the start point of the bandgap to its center. (d) Natural frequencies of the finite 1D topologically arranged mechanical metamaterial spring–mass lattice comprising 122 masses with auxetic hourglass metastructure k_a attached at both the adjacent sides of the interface mass exhibiting resonating and interface modes over the range of non-dimensional frequencies.

the value of stiffness parameter as $\gamma < 0$ and springs with stiffness lesser than the mean value attached at the adjacent sides of the interface mass results in interface mode which is obtained anywhere from center of the bandgap to the left-hand side of the bandgap depending on the value of γ parameter at the frequency $\Omega = \sqrt{3 - \sqrt{1 + 8\gamma^2}}$. It is observed that as the value of stiffness parameter γ changes from positive to negative, the symmetric mode obtained for $\gamma > 0$ within the bandgap gets converted into the localized anti-symmetric mode for $\gamma < 0$. The amplitude obtained at the interface mass is large enough than the desired one which can be used for various applications like energy harvesting. The localized interface mode obtained within the bandgap of the lattice structure resembles a sharp peak of base displacement and gives a better illustration of guiding the wave at a precise frequency. Implementing the hourglass metastructures, instead of linear springs at the position adjacent to the interface mass, we can have a new way of energy harvesting in topologically protected edge states with the help of hourglass lattice-based mechanical metamaterials due to the customizable stiffness of hourglass possible from the presence of lattice on its dome shape. The energy harvested would be dependent on the cell angle (θ_c) of the hourglass metastructures implemented in the topological metamaterial lattice. The stiffness of hourglass metastructures would correspond to honeycomb lattice when stiffness parameter $\gamma > 0$, and it would correspond to auxetic lattice when $\gamma < 0$. For distinguishing between bandgap and interface mode, we considered the periodic diatomic lattice without interface mass and without breaking symmetry which would result in the bandgap present in the frequency response function plot of the diatomic lattice where vibration can be isolated. For the realization of interface mode within the bandgap, we consider the lattice comprising 122 masses out of which 60 masses are on the left side of the interface unit cell corresponding to the left-hand diatomic
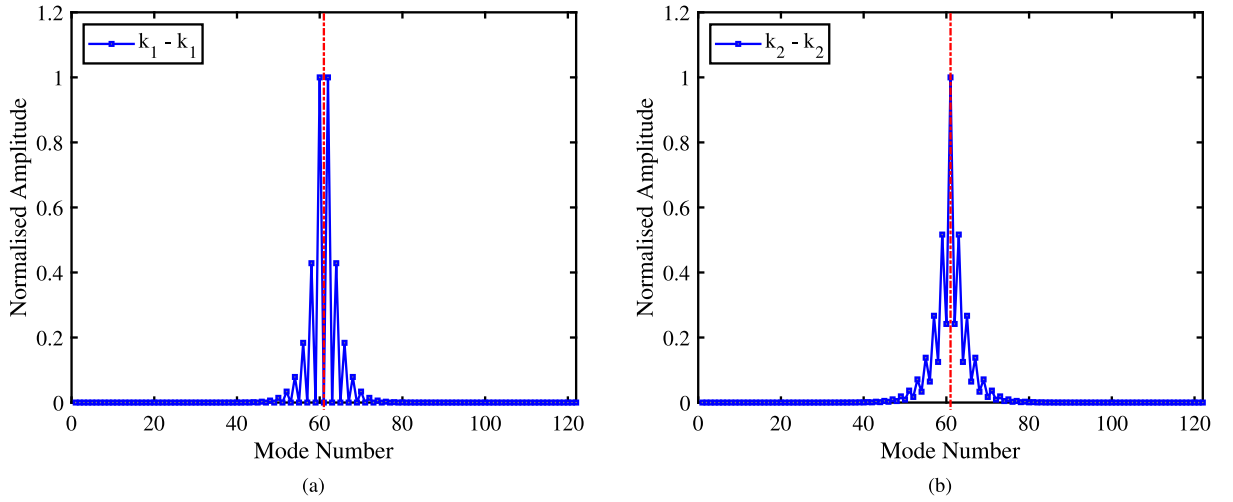
Fig. 4. Considering lattice with 122 masses attached using springs (a) Normalized amplitude versus mass mode number with the $k_1 - m - k_1$ arrangement at adjacent sides of interface mass having $\gamma = 0.4$ about the interface frequency at $\Omega = \sqrt{2}$. (b) Normalized amplitude versus mass mode number with the $k_2 - m - k_2$ arrangement at adjacent sides of interface mass having $\gamma = -0.4$ about the interface frequency at $\Omega = 1.2206$.

sublattice and 60 masses on the right side of the interface unit cell corresponding to right-hand diatomic sublattice. Since the system is one dimensional, we would assume the boundary conditions at the extreme left end of the sublattice is given a harmonic excitation displacement of $u_{w,-30} = \cos(\Omega\tau)$ for $(j = -30)$ while keeping the extreme right end of the sublattice free. The frequency response of the lattice is taken at the interface unit cell of the topological metamaterial lattice. The displacement for the center-mass can be obtained by formulating the eigenvalue problem given in Eq. (47). We observed that the regular diatomic lattice with identical masses and alternating springs does not support any localized modes within the bandgap. In the case where symmetry is broken, there is a localized mode obtained within the bandgap. The frequency at which the interface mode is obtained within the bandgap is predicted by the analytical solution, which is derived explicitly using Eq. (44). These frequencies support the localized interface modes for various arrangements of the lattice, i.e., $k_1 - k_1$ (hard-hard) or $k_2 - k_2$ (soft-soft) spring arrangement at the adjacent sides of the interface mass.

3. Experimental method

3.1. Additive manufacturing of 3D printed hourglass metastructure samples

The double dome of the hourglass metastructure is connected through the radial surface to avoid any stress concentration. The CAD model is converted to a STereoLithography file (STL) to fabricate additive manufactured samples. The 3D printing material PCTPE is flexible in nature, procured from Taulman 3D and utilized for printing the hourglass metastructure samples using Ultimaker 3.0 Extended 3D printer having a multi-material printing facility. The filament diameter of the PCTPE is 2.85 mm. The mechanical properties of PCTPE material are : density $\rho = 1.25$ gm/cm^3, Poisson's ratio $\nu = 0.285$, and Modulus of Elasticity $E = 73$ MPa, respectively. Specifications of 3D printing and its associated control parameters are provided in Table 1. Fig. 5 shows the three different types of 3D printed hourglass samples.

3.2. Dynamic testing of the hourglass samples

Non-contact vibration measurement techniques are adapted for measuring the dynamic response of hourglass metastructure. Three samples of the hourglass, namely regular honeycomb, auxetic, and solid shell were 3D printed and their responses were compared by carrying out dynamic testing using the 3D Laser Doppler Vibrometer (LDV) of Polytec. The samples were mounted on the Electrodynamic LDS shaker system (V201). The hourglass metastructure samples are attached to the aluminum plate at the top and bottom. The hourglass metastructures are placed between the two plates in a sandwiched manner upon which retro-reflective tape is attached which is used to reflect the incident laser beam, as shown in Fig. 6. Laser sensor heads recorded the velocity of the vibrating surface by measuring the phase shift of incident and reflected laser beam from it. At the same time, NI-DAQ systems are used for data acquisition and signal processing. Base excitation technique was used to determine the transmissibility of hourglass samples for which 1600 FFT lines with pseudo-random signal were provided by the LDS shaker. Experiments were performed for an excitation frequency range of 0 to 300 Hz, with two different gains of g = 1 and g = 1.6, and corresponding displacement readings of top and bottom aluminium plates of hourglass metastructure is recorded. In turn, from the measured data, transmissibility was calculated. The recorded data was post-processed with a Saitzky-Golay filter with frame length 5 and of order 1, thereby filtering
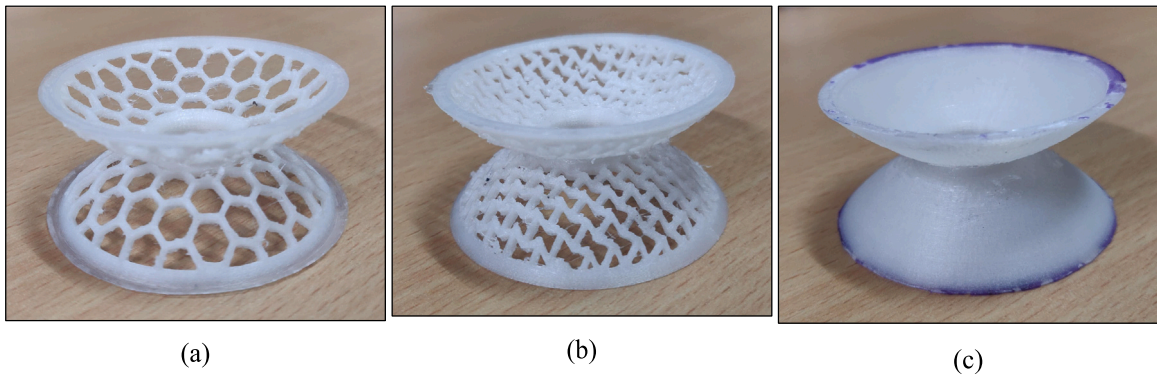
Fig. 5. 3D printed hourglass samples using PCTPE (Plasticized Copolyamide Thermoplastic Elastomer) material with different lattices namely (a) honeycomb (b) auxetic and (c) solidshell respectively. Hourglass metastructures with different cellular lattices are designed using the CAD modeling software SolidWorks with specified dimensions of the free height of the hourglass metastructure, H = 24 mm (the height of each dome is h = 12 mm). The spherical radius of domes is 40 mm, and the thickness in the radial direction is 2 mm, while the base radius is 38 mm.

Table 1
3D printing detailed specifications for hourglass metastructures.

| Sr. No.	Specifications in 3D printing	Value (unit)
1	3D Printing material	PCTPE 2.85 mm nominal diameter
2	Thickness of layer height	0.15 mm
3	Infill density	100%
4	Infill pattern	Triangular
5	Speed of printing	70 mm/s
6	Support placement	Support overhang angle 45 °C
7	Support pattern	Zig-zag (auxetic and solid shell) gyroid (honeycomb lattice)
8	Print temperature	240 °C
9	Temperature of Built plate	90 °C
10	Support density	20%
11	Support line distance, infill layer support line distance	2.5 mm (both)
12	Type of Built plate adhesion	Brim, raft
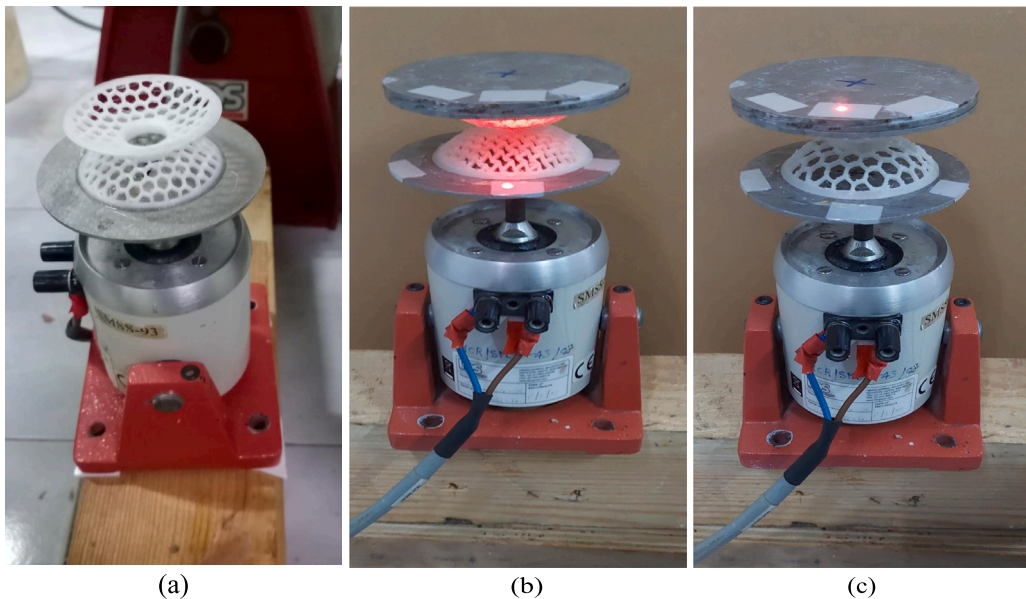
Fig. 6. (a), (b) and (c) shows dynamic testing of hourglass sample using LDS shaker up to frequency range of 300 Hz with the dead weight of 100 gm mounted at the top of hourglass sample with LDV laser beam incident.
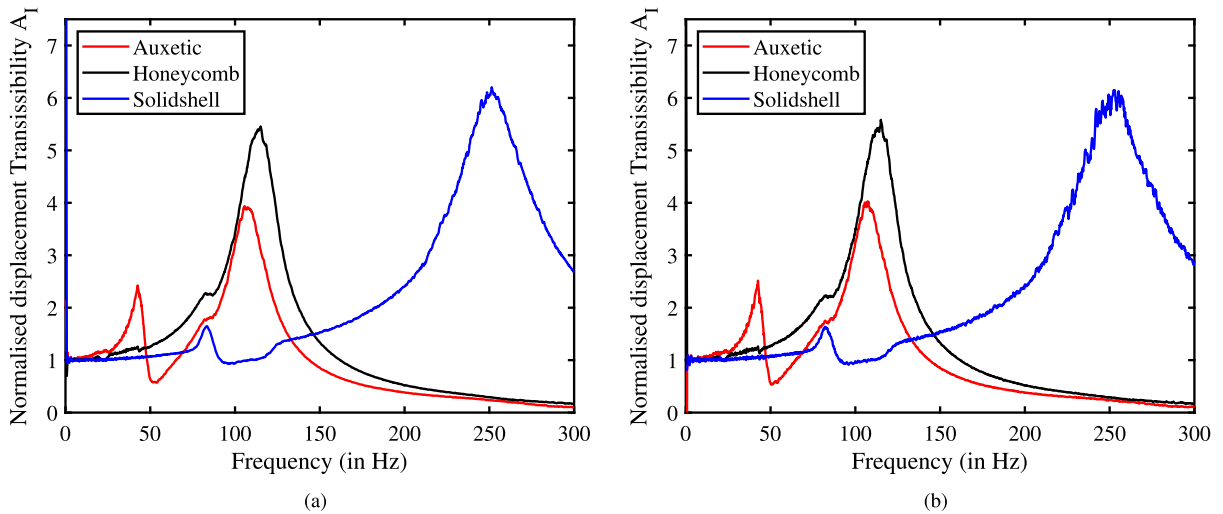
Fig. 7. 3D Hourglass printed samples dynamically tested using LDS shaker with LDV data acquisition system having gain (a) g = 1 and (b) g = 1.6 upto 300 Hz.

the noise. The dead weight of the aluminium plate mounted on the hourglass sample was 100 gm. The stiffness of the hourglass sample was measured by calculating the natural frequency of the fundamental mode. The peak frequency in Hertz for the auxetic, regular honeycomb, and solid shell obtained experimentally came out to be 105.5 Hz, 115 Hz, and 251.4 Hz, respectively, which can be verified from Fig. 7(a) and (b). The masses of hourglass metastructures were 6.05 gm, 4.97 gm, and 12.67 gm, respectively. Since the mass of hourglass is very small compared to the dead weight applied, the effect of mass of hourglass is neglected for natural frequency estimation. Accordingly, the stiffness of honeycomb, auxetic and solid shell hourglass were obtained as 52 N/mm, 43.94 N/mm, and 249.51 N/mm, respectively. The natural frequencies were obtained experimentally from the transmissibility plots through the base excitation technique.

3.3. Experimental setup of topological metamaterial

In order to obtain a non-trivial localized interface mode experimentally, we considered 12 periodic unit cells comprising 24 masses connected by springs of alternate stiffnesses, k_1 and k_2. The springs were designed of two different configurations, i.e., having different wire and coil diameters keeping the alternating stiffness as $k_1 = 825$ N/m and $k_2 = 175$ N/m. The masses are considered identical, each weighing 150 gm. The experimental setup consists of the system, which is manufactured considering the balancing aspect (dynamic and static), thereby not requiring any complex attachments to support it. The masses are supported by the cantilever support structure of considerable length such that when axial longitudinal vibrations are provided to the spring–mass chain, for small amplitude of vibrations, the motion is assumed to be in the longitudinal direction only. The guideway act as a frame for the masses attached with rigid link connections (with hinge joint), treated as a 1D pendulum chain for small angular deflections. The schematic of the complete experimental setup is shown in Fig. 8.

The metamaterial lattice, as shown in Fig. 9, comprises the two fixed guideways supported on the fixtures, and the chain of the coupled spring–mass system resembles a 1D pendulum chain. The optimum length for the system is calculated to be 2.5 m, and a total of 24 masses were on it. The objective of obtaining localized interface mode within the bandgap is well achieved theoretically as well as numerically using MATLAB and COMSOL simulations. The experimental setup was designed as per the proposed schematic diagram of the experimental setup in Fig. 9; the different components were manufactured and assembled to carry out experiments, as shown in Fig. 10. In order to achieve the one-dimensional spring–mass chain motion in the horizontal direction, all the masses are suspended from the fixed end and rigidly supported using guideways by a reasonably large length cantilever support such that they behave as pendulums individually. The complete system resembles a compound pendulum, and during the operation, the possibility of the effect of the small angle of tilt of each mass from a horizontal position can be neglected so that the 1D model can be assumed. The cantilever support shown in Figs. 9 and 10 are of rectangular cross-section so that due to its high moment of inertia in torsion, the lateral movement of topological metamaterial spring–mass system can be constrained in one direction only.

4. Results and discussion

4.1. FEA simulation of topological metamaterial lattice

In order to identify the bandgap occurrences via simulation, a one-dimensional periodic diatomic lattice with 122 masses and alternating springs is first explored in the absence of interface mass without breaking symmetry. The frequency response function (FRF) and phase diagram are obtained using the lumped mechanical system model in COMSOL, the excitation is given at one end
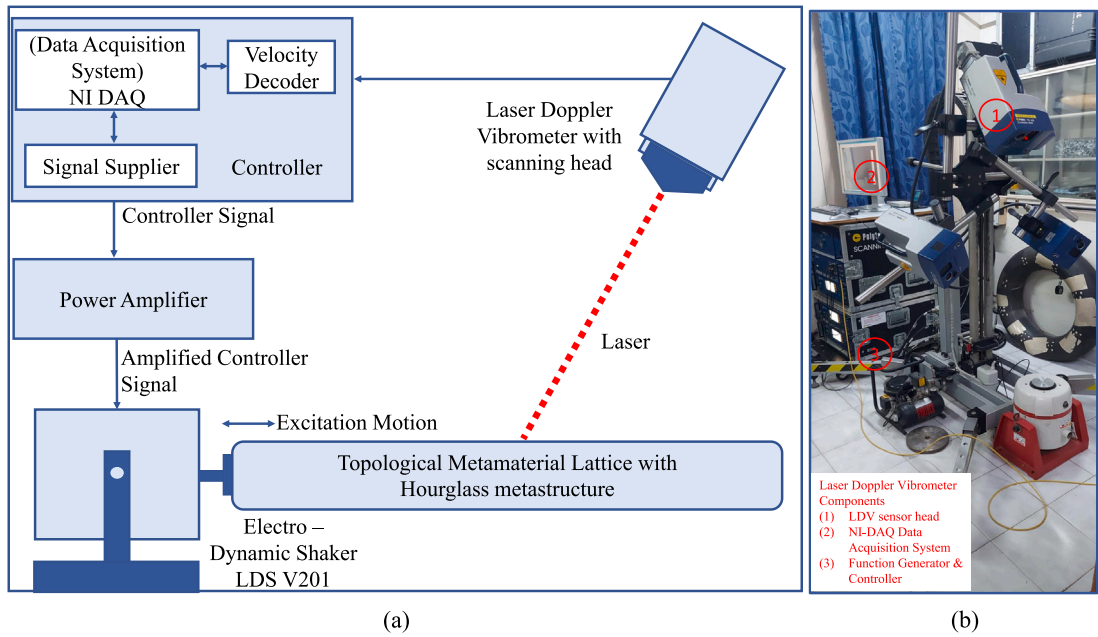
Fig. 8. (a) Schematic diagram of the experimental setup with topological metamaterial lattice along with interface mode (b) Laser Doppler Vibrometer.
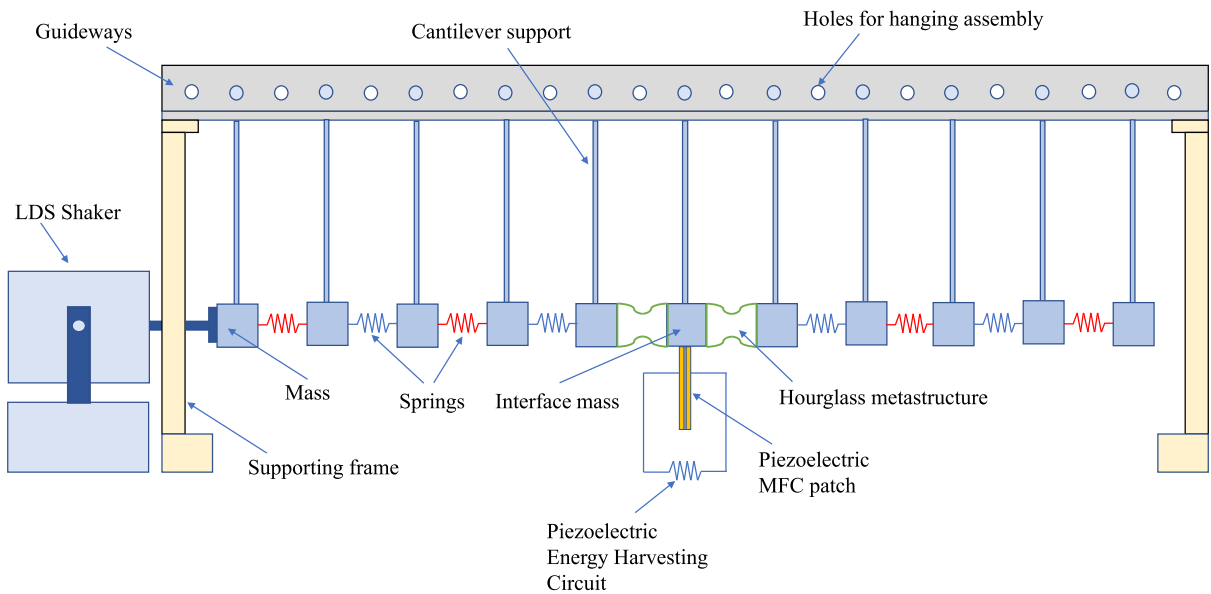

Fig. 9. Conceptual schematic diagram of topological metamaterial lattice with hourglass mounted at the adjacent sides of the interface mass along with integrated piezoelectric energy harvesting circuit.

of the lattice keeping the other end free, and response is measured at the interface mass. The bandgap is evident in the frequency response function plot and is further confirmed by phase plot, which reveals no phase change in the bandgap, as shown in Fig. 11(a) and (b) respectively.

The FEA simulation of topological metamaterial lattice comprising 61 unit cells, out of which 30 unit cells are on the left sub-lattice, and 30 unit cells on the right sub-lattice with the central unit cell acting as an interface, i.e., with 122 identical masses m and alternating springs k_1 and k_2 attached sequentially with a broken symmetry at the interface mass is performed in COMSOL, and the frequency response is obtained thereby verifying the presence of localized interface mode at the same frequency as obtained using the analytical formulation. Harmonic excitation is given at one end of the lattice keeping the other end free, while the response was calculated at the interface mass. The simulations with springs at the adjacent sides of interface mass for two different types
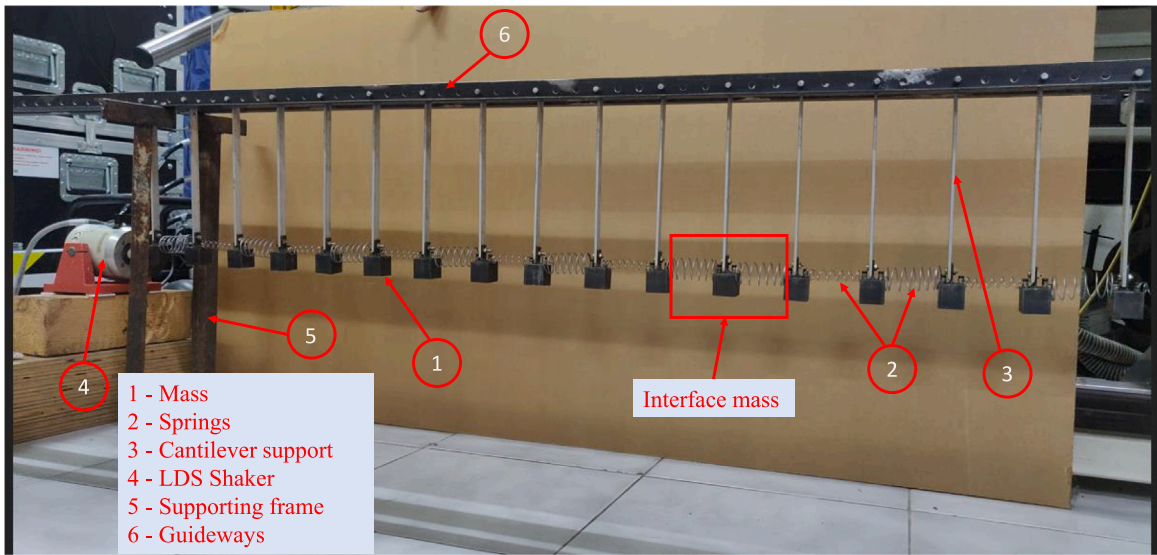
Fig. 10. Experimental setup of topological metamaterial lattice with hard-hard springs arrangement at adjacent sides of interface mass i.e. $k_1 - k_1$ to demonstrate interface mode.
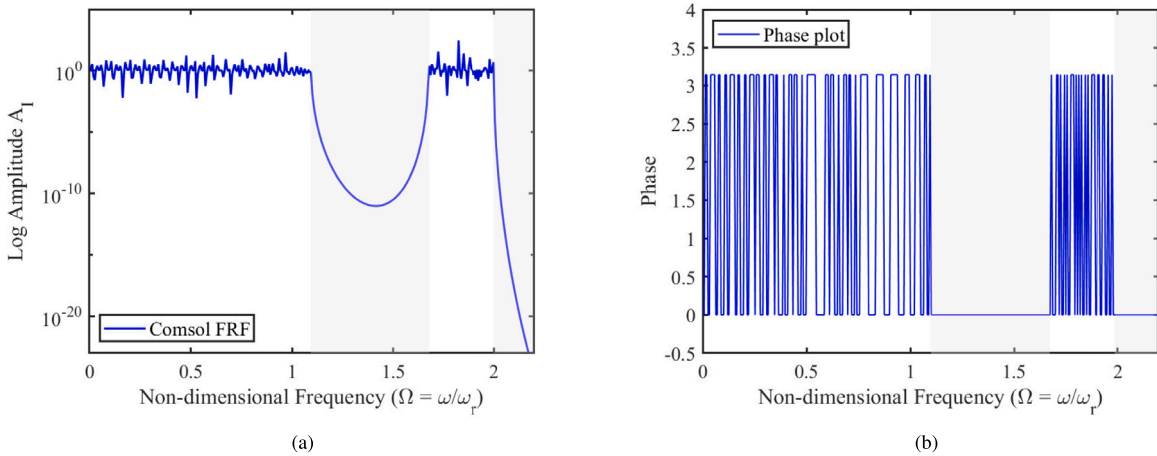

Fig. 11. 1D diatomic spring–mass lattice subjected to harmonic excitation at one end keeping other end free while response measured at center mass (a) Frequency Response Function in COMSOL and (b) Phase plot in COMSOL. The parameters considered are : $m = 1$ kg, $k = 1$ N/m, $k_1 = k(1 + \gamma)$, $k_2 = k(1 - \gamma)$, $\gamma = 0.4$.

of arrangements, i.e. hard-hard $(k_1 - k_1)$ and soft-soft $(k_2 - k_2)$ springs, are carried out. Hourglass metastructure with honeycomb and auxetic cells were placed at the adjacent sides of interface mass, considering linear stiffness. With the help of simulations, it is possible to study the frequency response function and phase plot when auxetic hourglass and regular honeycomb hourglass lattices are coupled next to the interface mass under the linear stiffness assumption as shown in Fig. 12. The modified topological metamaterial is having different stiffness adjacent to interface mass governed by χ parameter, with χ being any scalar value. It is observed that with an increasing value of χ, for $\gamma < 0$ lattice arrangement case at neighboring sides of a topological lattice, the generalized case of a modified lattice with interface mass under consideration would cause the interface mode frequency to move from left to right. For the modified topological lattice with added χ parameter for $\gamma > 0$, the interface mode at $\Omega = \sqrt{2}$, obtained at symmetric mode, would not change.

The experimental FRF results obtained by attaching 24 identical masses $m = 150$ gm along with the alternating springs having stiffness $k_1 = 825$ N/m and $k_2 = 175$ N/m and $\gamma = 0.65$ for topological metamaterial lattice with hard-hard $(k_1 - k_1)$ spring arrangement at the adjacent sides of interface mass clearly show good agreement of the localized interface mode obtained via simulation in COMSOL where same parameters were used and results match within the bandgap as shown in Fig. 13.

The response is measured at the interface mass unit cell i.e. second mass of the interface unit cell where displacement obtained is maximum. It is observed that damping conditions are present, and the amplitude of side resonating masses is reduced to some
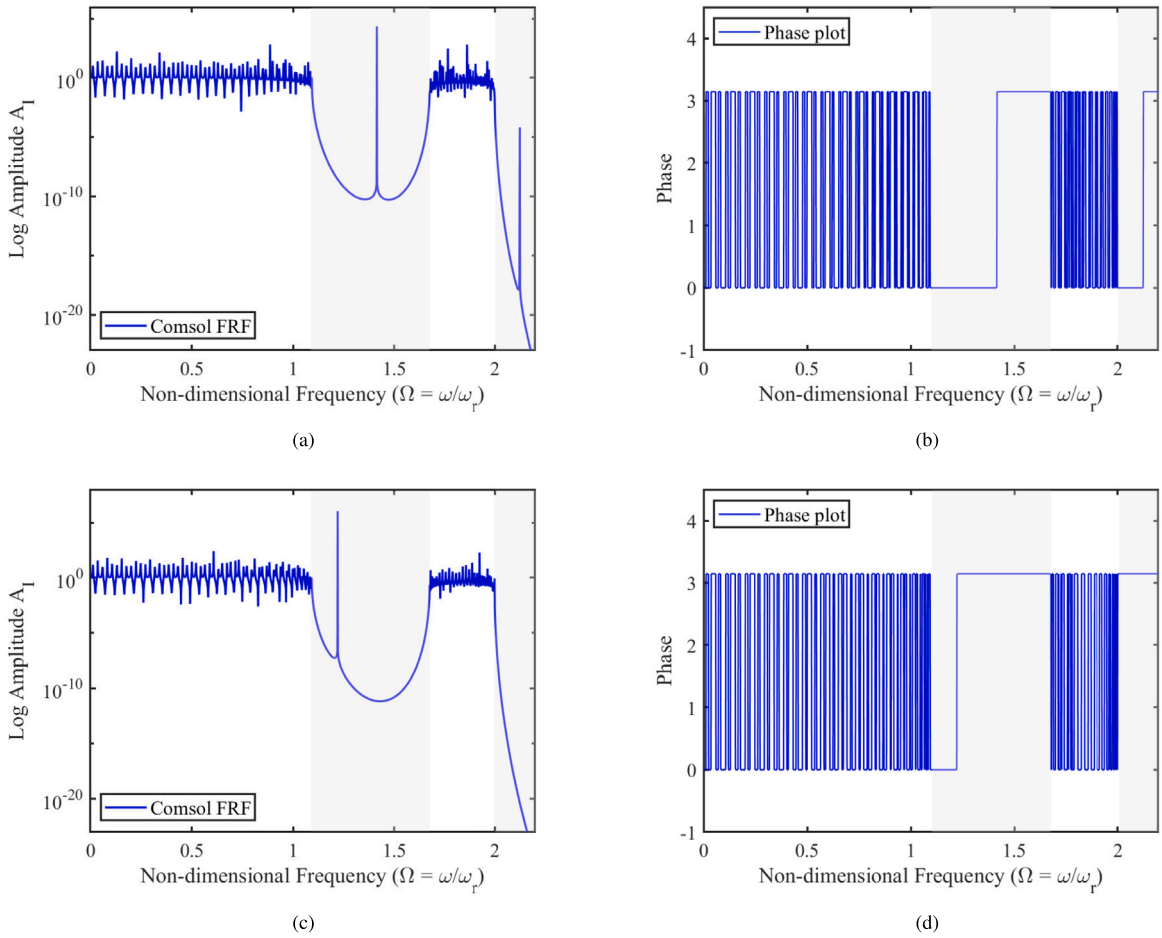
Fig. 12. 1D topological metamaterial spring–mass lattice subjected to harmonic excitation at one end keeping other end free while response measured at center mass when regular honeycomb hourglass structure k_h or auxetic hourglass structure k_a is attached adjacent to interface mass. (a),(c) Frequency Response Function in COMSOL and (b),(d) Phase plot in COMSOL for regular honeycomb and auxetic hourglass respectively. The parameters considered are : $m = 1$ kg, $k = 1$ N/m, $k_1 = k(1 + \gamma)$, $k_2 = k(1 - \gamma)$, $\gamma = 0.4$ for regular honeycomb hourglass adjacent to interface mass, while $\gamma = -0.4$ for auxetic hourglass adjacent to interface mass.

extent rather than on the interface mass, as shown in the experimental plots. Fig. 13(b) clearly depicts the localized interface mode present within the bandgap located at the center of the bandgap. The analysis is carried out in a low-frequency range i.e. from 0 to 25 Hz, which is our area of interest. The interface mode is obtained at the frequency of 12.64 Hz when the frequency response function is plotted as a transmissibility plot i.e. ratio of the response signal and base excitation signal. While Fig. 13(b) represents the comparison of FRF plots obtained from COMSOL as well as experimentally obtained FRF plots, which shows good agreement with each other. This study is majorly focused on the interface mode obtained within the bandgap. Thus the interface mode above the optical mode is not explored in this case. Furthermore, the phase plot for the same obtained in COMSOL can be observed, as shown in Fig. 13(c), which agrees with the presence of localized interface mode at the center of the bandgap, indicated by a single blue-colored line inside the gray color of the bandgap.

4.2. Energy harvesting within the bandgap

We obtained a localized interface mode within the bandgap by incorporating hourglass metastructure in topological metamaterial lattice within the adjacent sides of interface mass. The dependence of the cell lattice angle (θ_c) of hourglass metastructure was found to affect energy harvesting significantly. The amplitude obtained at the localized interface mode, where the symmetry of lattice is broken, is of high magnitude from which energy harvesting is carried out and can be utilized to power the electronic devices within the bandgap. The voltage and power plots obtained by integrating a cantilevered bimorph piezoelectric energy harvester give us the implications of the voltage and power obtained corresponds to the fundamental mode, as shown in Fig. 14. The properties of the macro fiber composite along with the dimensions taken into consideration, are provided in Table 2.

Similar experimentation is performed with soft-soft ($k_2 - k_2$) spring arrangement at adjacent sides of interface mass as shown in Fig. 15(a) and the unit harmonic excitation displacement is given at base mass, keeping another end free, and response is measured
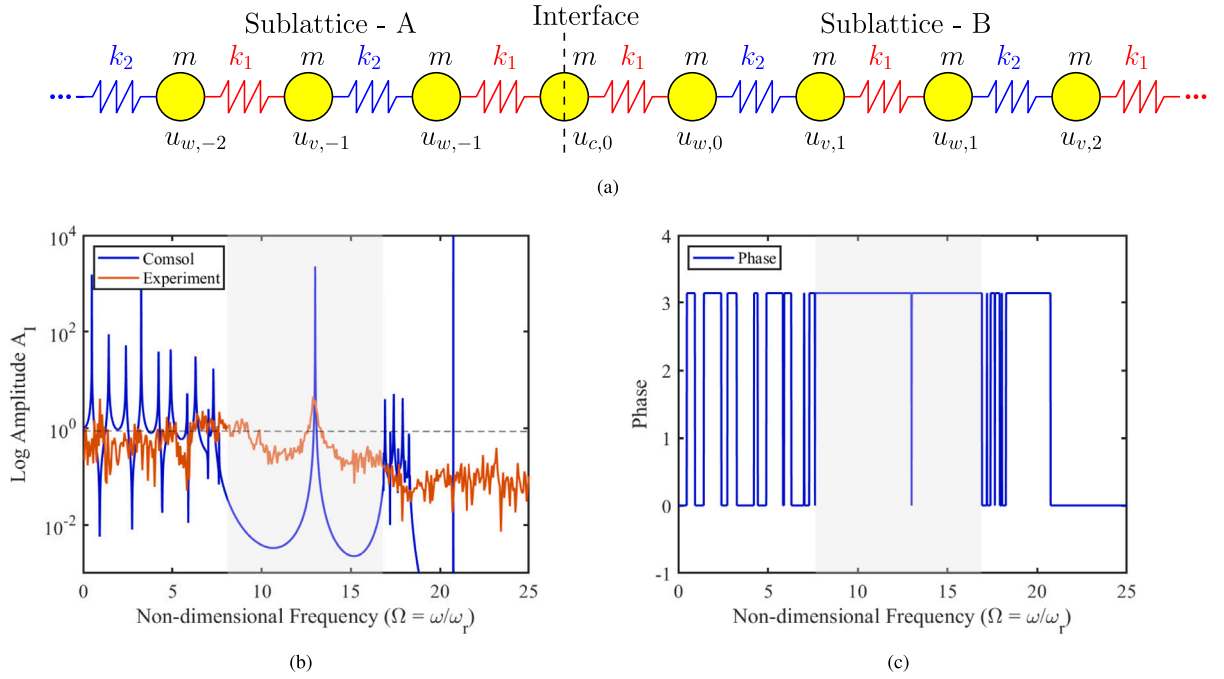
Fig. 13. (a) Schematic diagram of topological metamaterial lattice with hard-hard $(k_1 - k_1)$ springs attached at adjacent sides of interface mass excitation given at one end and response measured at interface. The parameters considered are : $m = 150$ gm, $k_1 = 825$ N/m, $k_2 = 175$ N/m. (b) Experimental and COMSOL FRF comparison showing interface mode at 12.64 Hz for hard-hard $(k_1 - k_1)$ arrangement (c) Phase plot for hard-hard $(k_1 - k_1)$ arrangement in COMSOL depicting interface mode phase change within the bandgap at same frequency. (For interpretation of the references to color in this figure legend, the reader is referred to the web version of this article.)

Table 2
Piezoelectric material properties : MFC M-2814-P1.

Sr. No.	Property parameter	Value
1	Length of piezo (L_p)	118 mm
2	Width of piezo (W_p)	35 mm
3	Height of piezo (t_p)	0.08 mm
4	density (ρ_p)	5650 kg/m³
5	Capacitance of each layer (C_p)	15.11 nF
6	Series connection (χ)	0.5
7	d_{31}	−170 pC/N or pm/V
8	d_{33}	374 pm/V
9	Young's modulus of piezo (E_p)	30.336 GPa

at interface mass unit cell, i.e. first mass of interface unit cell where the displacement obtained is maximum for this case. A good agreement is achieved with experimental frequency response function plots and simulation results on the presence of the interface mode within the bandgap, which is found to be shifted slightly towards the left side from the center of the bandgap. The considered masses are identical $m = 150$ gm and stiffness of springs $k_1 = 825$ N/m and $k_2 = 175$ N/m. Localized interface mode of this lattice is obtained at a frequency of 9.56 Hz. However, both plots give a clear idea of the shifting of interface mode towards the left side from the center of the bandgap, as shown in Fig. 15(b) and (c). Using a bimorph cantilevered piezoelectric energy harvester attached to the interface mass as formulated [51,52]. The peak voltage is obtained at the same frequency at which the interface mode is obtained, as shown in Fig. 16(a) and (b), representing peak experimental voltage and comparison of experimental and analytical voltage. Thus, by appropriately choosing the dimensions of the bimorph cantilevered PZEH such that the fundamental mode of the cantilever occurs at the same frequency at which the interface mode has appeared within the bandgap and by utilizing its high amplitude available at the interface mass, one can obtain the value of voltage. The maximum value of experimental voltage and power available for $(k_2 - k_2)$ configuration as depicted in Fig. 16(a) and (b) is 12.59 mV and 0.062 µW respectively when connected with a load resistance of 2500 Ω in series. In addition to that, the FRF and phase plot provide a good agreement of the interface mode shifting towards left side from the center of the bandgap.
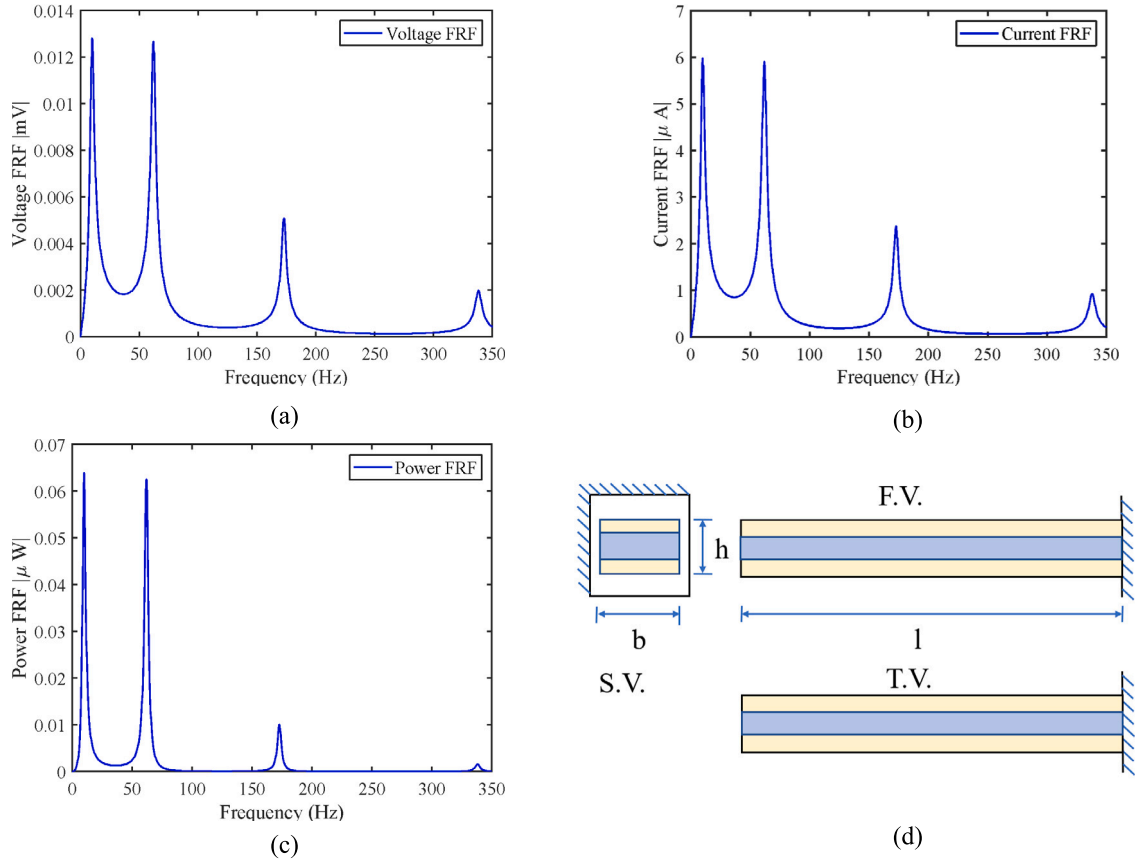
Fig. 14. Analytically calculated (a) Voltage (b) Current (c) Power plots for cantilever bimorph piezoelectric energy harvester subjected to harmonic base excitation. (d) Schematic representation of cantilever bimorph PZEH.

4.3. Generalized case of modified lattice with interface mass and experimental validation

Hourglass metamaterial lattice with modified spring stiffness mounted from both sides of interface mass, whose stiffness is governed by the stiffness tuning parameter χ, is schematically represented in Fig. 17. In order to consider a generalized case, where the placement of different stiffness of springs is allowed at the adjacent sides of interface mass other than k_1 or k_2, the new stiffness is denoted by expression $k_3 = \chi k_1$, and corresponding analytical expressions are derived. Subsequently, the experimental validations are also presented.

We have performed analytical solution for eigenfrequency and displacement of the Nth unit cell for modified topological lattice. Considering the overall height of hourglass as 24 mm and single dome height of 12 mm. The governing equation of the interface mass with modified stiffness is given by

$$m\ddot{u}_{c,0} + \chi k_1 (2u_{c,0} - u_{w,-1} - u_{w,0}) = 0 \tag{48}$$

$$-\Omega^2 u_{c,0} + \chi(1+\gamma)(2u_{c,0} - u_{w,0} + u_{w,-1}) = 0 \tag{49}$$

The localized interface mode is obtained for different values of the modified spring stiffness mounted adjacent to interface mass. The displacement relationship for any unit cell on sublattice - B and interface mass unit cell as well as that between any unit cell on sublattice - A and interface mass unit cell of modified topological metamaterial can be obtained from Eq. (A.1.15) in Appendix A.1 and Eq. (A.2.30) in Appendix A.2 respectively.

Computation of the exact resonant natural frequencies or mode shapes for modified topological metamaterial lattice analytically leads to complex calculations. As a result, the closed form resonant frequency for modified topological lattice cannot be obtained. It is dependent on the value of χ and number of unit cells taken into account for given range of γ. The interface mode frequency of the modified topological lattice with definite number of unit cells for varying values of γ is obtained by investigating the governing equation of interface mass mentioned in Eqs. (48) and (49), and its corresponding mode shape for different values of χ, as shown in Fig. 18. The outer curves shown in red and blue color specifies the limits bounding the interface mode frequency for different values of χ. The displacement amplitude of interface mode for modified topological metamaterial lattice acquired on
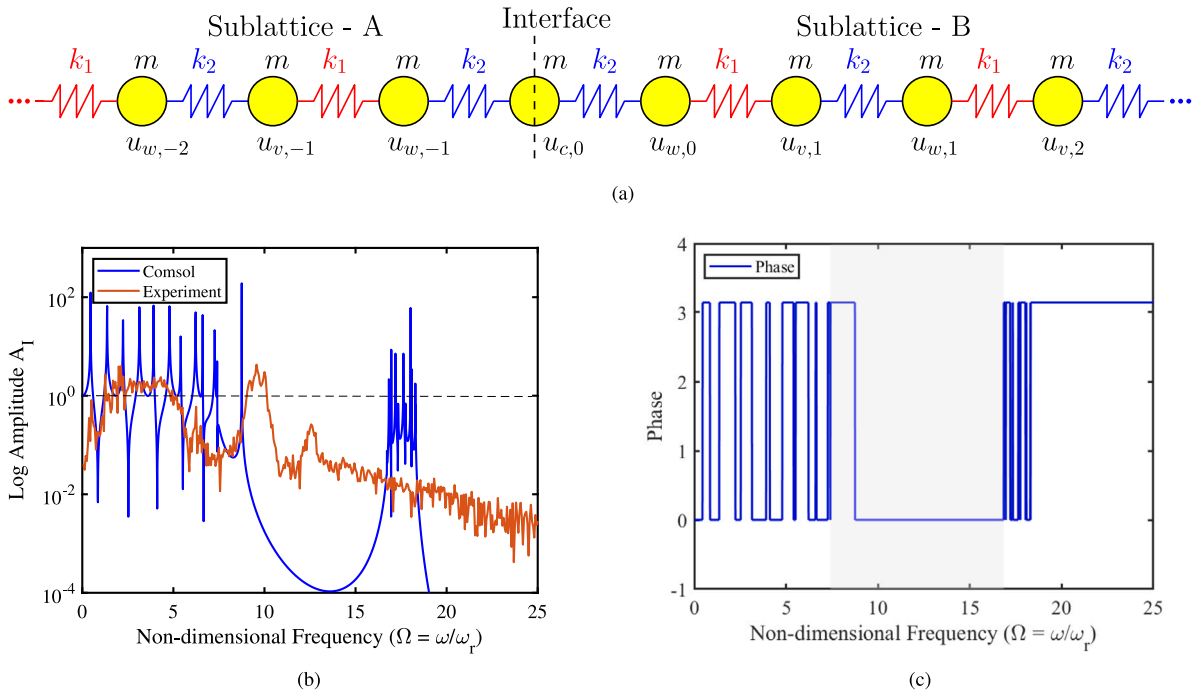
(a)

(b)

(c)

Fig. 15. (a) Schematic diagram of topological metamaterial lattice with soft-soft $(k_2 - k_2)$ springs attached at adjacent sides of interface mass excitation given at one end and response measured at interface. The parameters considered are : $m = 150$ gm, $k_1 = 825$ N/m, $k_2 = 175$ N/m. (b) Experimental and COMSOL FRF comparison showing interface mode at 9.56 Hz for soft-soft $(k_2 - k_2)$ arrangement (c) Phase plot for soft-soft $(k_2 - k_2)$ arrangement in COMSOL depicting interface mode phase change within the bandgap at same frequency.
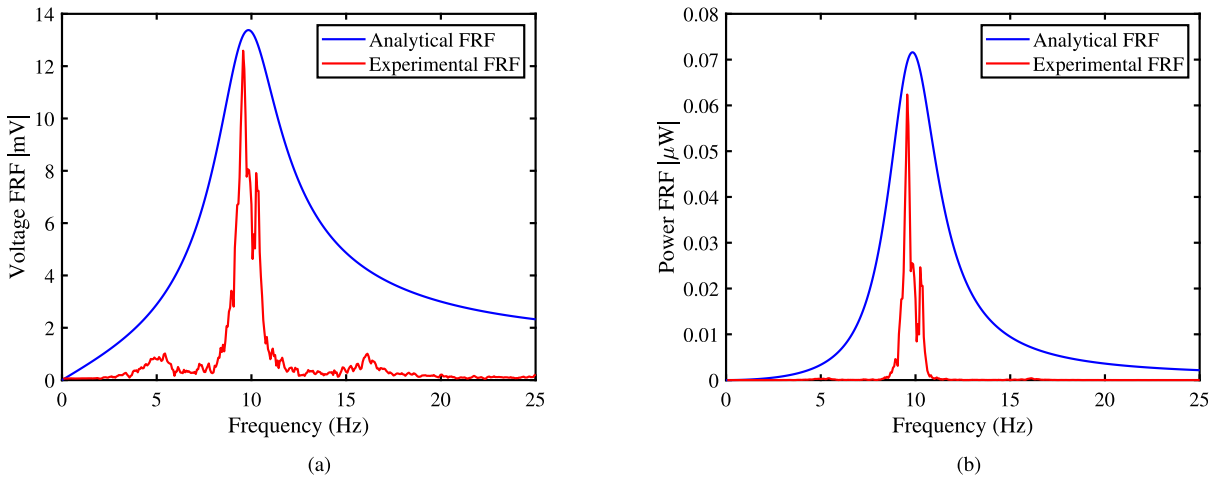

(a)

(b)

Fig. 16. Topological metamaterial lattice with soft-soft $(k_2 - k_2)$ spring arrangement attached at the adjacent sides of interface mass along with the piezobeam attached to it for voltage and power measurement showing peak at 9.56 Hz (a) Comparison between experimental and analytical Voltage FRF (b) Comparison between experimental and analytical Power FRF.
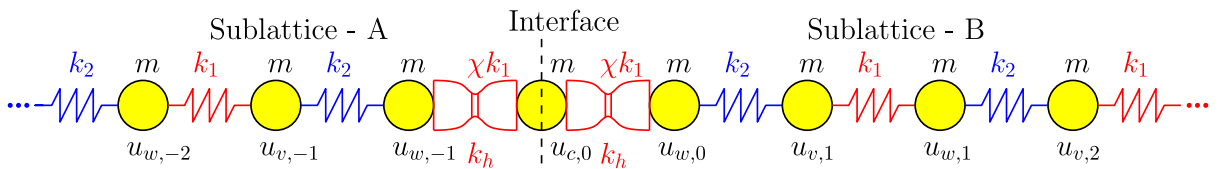

Fig. 17. 1D topological metamaterial lattice having diatomic unit cells comprising identical masses m and inversion symmetry broken at the interface with hourglass metastructure having stiffness $k_h = \chi k_1$ while the remaining lattice is connected with the linear springs having stiffness k_1 and k_2, where $k_1 = k(1 + \gamma)$, $k_2 = k(1 - \gamma)$, $\gamma = -0.4$.
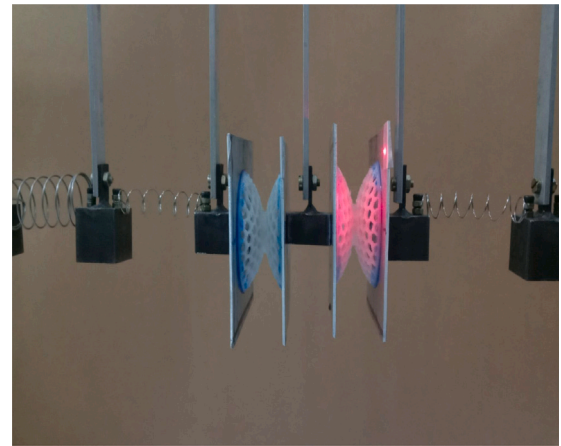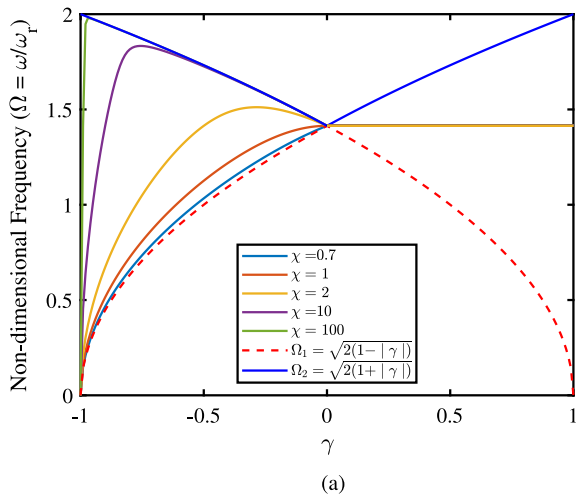
(a)   (b)

Fig. 18. (a) Plot of interface mass frequency versus γ parameter for different values of χ for the modified interface mass lattice consideration where $\chi = 0.7, 1, 2, 10$ and 100. Curves in red and blue color shows limits of frequencies that bound bandgap for lattice. (b) Representation of modified topological lattice with interface mass sandwiched by hourglass on adjacent sides. (For interpretation of the references to color in this figure legend, the reader is referred to the web version of this article.)
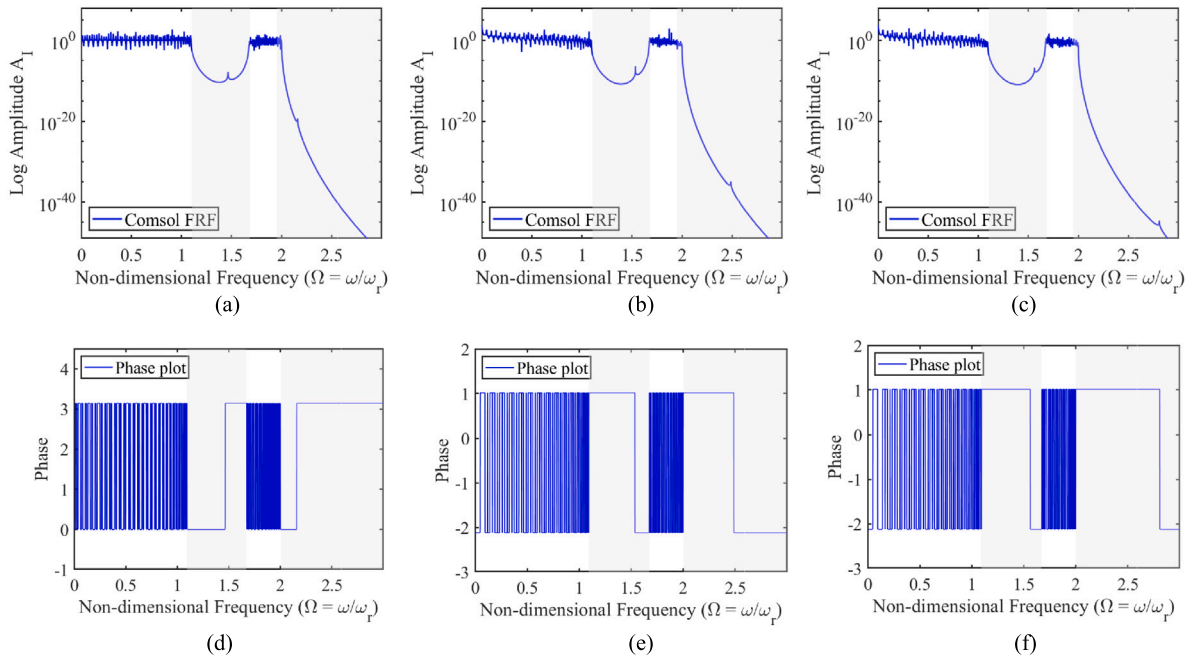

(a)   (b)   (c)

(d)   (e)   (f)

Fig. 19. COMSOL simulation for 1D diatomic modified topological metamaterial lattice having symmetry broken at the interface when hourglass auxetic metastructure k_a or $k_3 - k_3$ i.e. $(\chi k_1 - \chi k_1)$ springs are attached adjacent to interface mass along with excitation given at one end and response is taken at the interface. (a), (b) and (c) Frequency Response Function corresponding to modified stiffness parameter as $\chi = 2, 3$ and 4 respectively. (d), (e) and (f) Phase plot corresponding to modified stiffness parameter as $\chi = 2, 3$ and 4 respectively. The parameters considered are : $m = 1$ kg, $k = 1$ N/m, $k_1 = k(1 + \gamma)$, $k_2 = k(1 - \gamma)$, $\gamma = -0.4$.

logarithmic displacement scale is very small due to unavailability of the exact resonant frequency expression. To confirm existence of the interface mode in modified topological lattice and determine corresponding resonant frequencies, phase diagrams and their inflection points are obtained as shown in Fig. 19.

For further analysis of the system using COMSOL and validate the same through experimental FRF, modified topological metamaterial lattice $(k_3 - k_3)$ i.e. $(\chi k_1 - \chi k_1)$ arrangement was considered as $k_3 = k_a = 43{,}500$ N/m while keeping m, k_1 and k_2 unchanged. The COMSOL simulation results are shown in Fig. 19 and the validation with respect to the experimental results are shown in Fig. 20. The localized interface mode for this lattice having 24 masses came out to be at frequency of 15.63 Hz which is
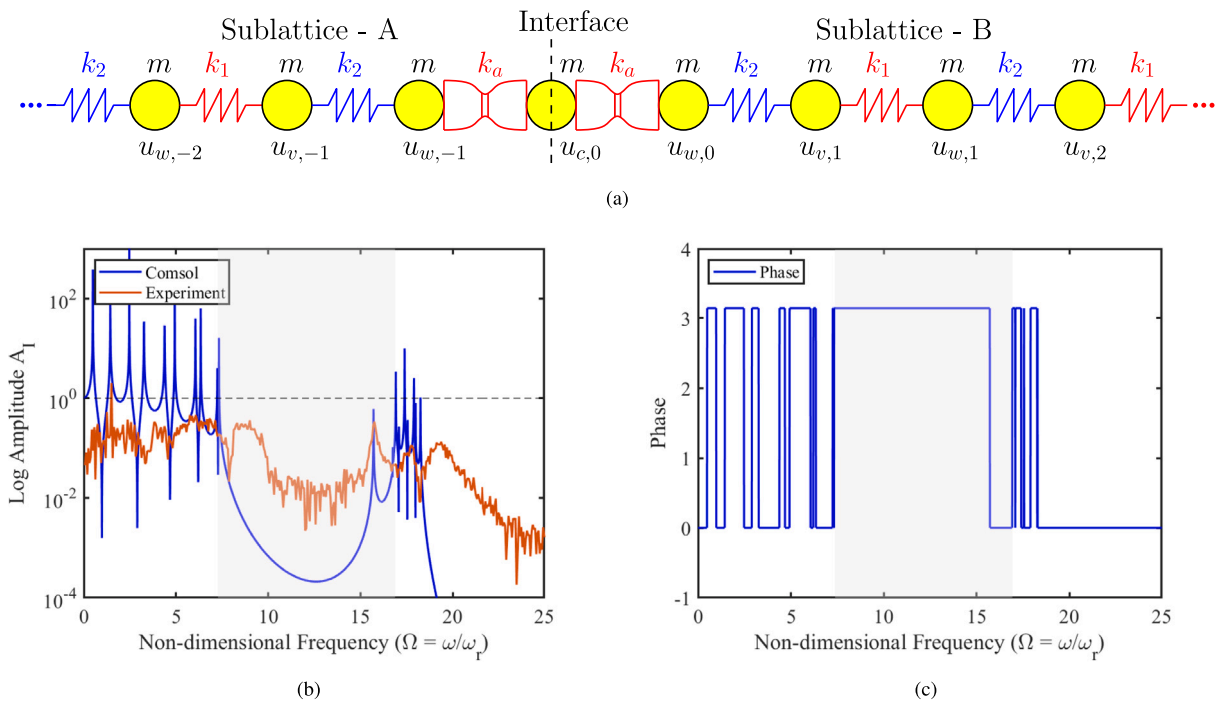
Fig. 20. (a) Schematic diagram of modified topological metamaterial lattice with auxetic hourglass metastructure having stiffness $k_a = k_3 = \chi k_1$ where χ is a parameter with $k_3 - k_3$ arrangement at the adjacent sides of interface mass with excitation given at one end and response measured at interface. The parameters considered are : $m = 150$ gm, $k_1 = 825$ N/m, $k_2 = 175$ N/m, $k_3 = 43,500$ N/m, $\chi \approx 50$. (b) Experimental and COMSOL FRF comparison showing interface mode at 15.63 Hz for modified lattice $(k_3 - k_3)$ arrangement (c) Phase plot for modified lattice $(k_3 - k_3)$ arrangement in COMSOL depicting interface mode phase change within the bandgap at same frequency.
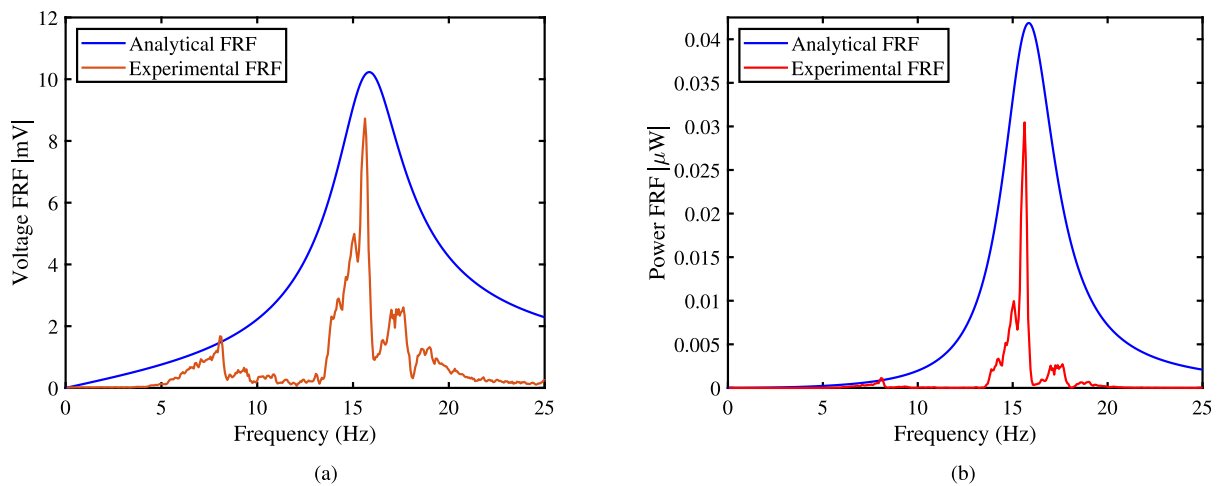

Fig. 21. Modified topological lattice with $(k_3 - k_3)$ auxetic hourglass arrangement at adjacent sides of interface mass having stiffness parameter $\chi \approx 50$ along with the piezobeam attached to the interface mass for voltage and power measurement showing peak at 15.63 Hz (a) Comparison between experimental and analytical Voltage FRF (b) Comparison between experimental and analytical Power FRF.

in good agreement with that obtained from FRF and phase plot in COMSOL which is presented in Fig. 20(b) and (c). The interface mode with increase in χ is observed to be shifting towards the right bands in the COMSOL simulation. The experimental peak voltage and power for modified topological lattice is found to be 8.72 mV and 0.03 μW respectively for load resistance of 2500 Ω in series and its comparison with the analytical solution for PZEH bimorph cantilevered beam is shown in Fig. 21(a) and (b), which are found to be in good agreement. As depicted in Fig. 20, simulations show significant amplification of peaks when compared to the experimental response. This amplification is primarily caused by not considering the damping effects due to friction and

Table 3

Stiffness comparison for distinct parameters of hourglass metastructures.

Type	θ_c	h	t	h/t	M	K
Auxetic	−72.169	24	2	12	0.7877	41.60×10^3
Auxetic	−75.5	24	2	12	0.7877	38.93×10^3
Auxetic	−72.169	24	3	8	0.7877	64.68×10^3
Auxetic	−75.5	24	3	8	0.7877	60.53×10^3
Honeycomb	+29.984	24	2	12	0.7877	48.70×10^3
Honeycomb	+30.015	24	2	12	0.7877	52.52×10^3
Honeycomb	+29.984	24	3	8	0.7877	75.71×10^3
Honeycomb	+30.015	24	3	8	0.7877	81.66×10^3
Solidshell	–	24	2.7	≈ 12	–	237.81×10^3
Solidshell	–	24	2.75	≈ 12	–	251.50×10^3
Solidshell	–	24	3.5	≈ 8	–	236.57×10^3
Solidshell	–	24	3.6	≈ 8	–	257.84×10^3

Table 4

γ parameter dependence on lattice of different hourglass metastructures.

Configuration of springs at adjacent sides of interface		$\frac{h}{t}$	θ_1	θ_2	k_1	k_2	γ / χ	Towards left bulk bands	Center of Bandgap	Towards right bulk bands	Frequency in Hz from COMSOL
$k_1 - m - k_1$ (Hard-hard)		2	+29.984	–	48,700	25,000	0.3125		■		111.5
		2	+30.015	–	52,500	25,000	0.3550		■		114.5
		3	+29.984	–	75,710	25,000	0.5035		■		130.3
		3	+30.015	–	81,660	25,500	0.5312		■		134.1
$k_2 - m - k_2$ (Soft-soft)		2	–	−72.169	25,000	41,600	−0.5	■			84.1
		2	–	−75.50	25,000	38,930	−0.5250	■			80.8
		3	–	−72.169	25,000	64,680	−0.3180	■			111.9
		3	–	−75.50	25,000	60,530	−0.3474	■			107.4
	k_3						χ				
$\chi k_1 - m - \chi k_1$ ($k_3 - m - k_3$) (Generalized case)	2,37,810	2	+29.984	−72.169	48,700	25,000	4.8831			■	123.5
	2,51,500	2	+30.015	−75.50	52,520	25,000	4.7886			■	128.7
	2,36,570	3	+29.984	−72.169	75,710	25,000	3.1268			■	150.1
	2,57,840	3	+30.015	−75.50	81,660	25,000	3.1574			■	155.5

viscoelastic energy dissipation of the hourglass material [29,53]. Additionally, presence of system noise represents a major cause of signal distortion.

Theoretical load–deflection profile dependent upon constitutive cell angle (θ_c) mentioned in Eq. (12) is considered to evaluate stiffness (approximated to be linear for small deflection) of the hourglass metastructure system as the same is incorporated in Table 3. The parameter γ is then examined for tunable frequency-dependent interface modes that span the system's bandgap from lower to upper frequency bands. The interface mode is found to be at the centre of the bandgap for honeycomb lattice metastructure with assumed linear alternating stiffness at remaining places, and is observed to be shifting towards left (lower frequency band) for auxetic lattice metastructure with same alternating stiffness. Table 4 shows a range of γ values together with related stiffnesses (k_1, k_2) at respective cell angles (θ_1 and θ_2). The location of the interface mode and the corresponding frequency have been underlined and categorized. Table 4 also specifically refers to the modified stiffness case for the ($k_3 - k_3$) arrangement, which has the stiffness of the hourglass metastructure of higher magnitude, and which causes the interface mode to shift towards the right (higher frequency band).

Combining piezoelectric or magnetostrictive materials with the hourglass presents a promising opportunity for active mechanical response tuning. By introducing the hourglass into the topological metamaterial lattice with remotely regulated stiffness variation, a shift in the interface mode frequency can be observed digitally within the bandgap. The synclastic curvature of the hourglass dome, which depends on geometrical parameters, can be actively controlled to achieve tunability of the interface mode within the bandgap. With the utilization of NiTiNoL-based SMA actuators or piezo stacks, it is possible to pre-stress the hourglass and dynamically adjust the stiffness actively. This advancement in the development of remotely controlled metamaterials enables the realization of active tuning of interface mode through hourglass integration.

There are enormous applications of this concept in terms of developing localized modes for vibro-acoustic devices that can be used for medical imaging as well as for developing transducer. The same system can also be used for energy harvesting from vibration. One potential application is the sensitivity of topological structures to the introduction of defects. By carefully positioning topological interfaces, waves can be customized and isolated, leading to a variety of potential applications in areas such as acoustic focusing, impact mitigation, sensing, and noise control [40]. Manipulating finite interface frequency modes in elastic topological structures has direct implications for structural health monitoring, energy transport, waveguiding without backscattering loss, wave tunneling,
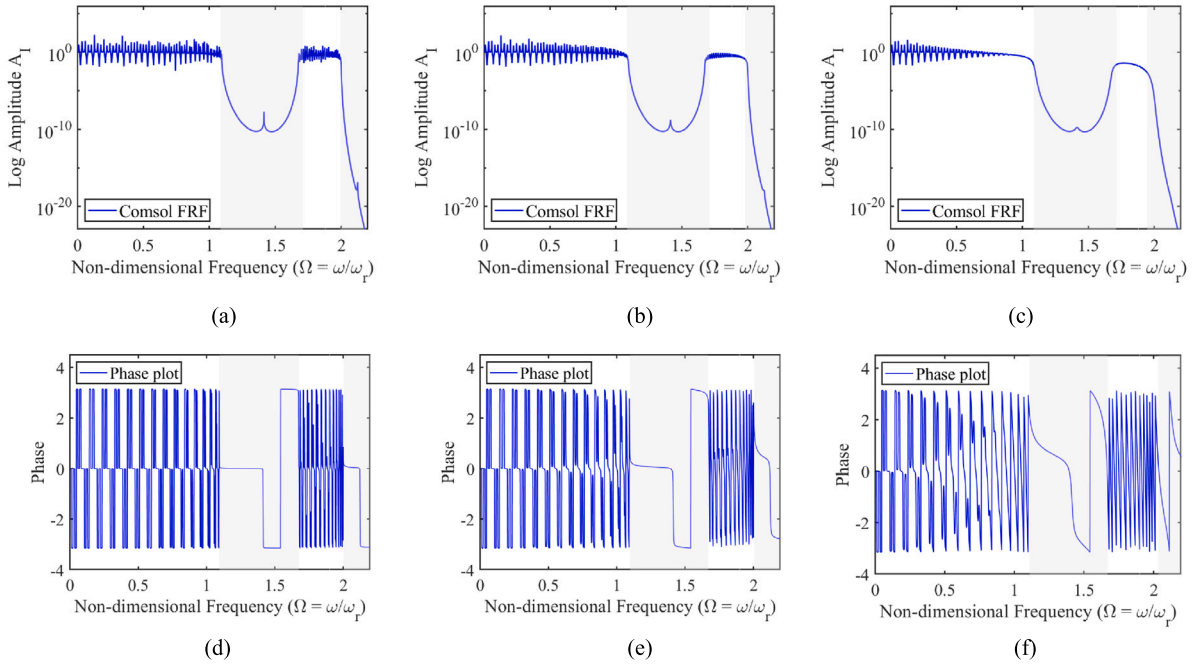
Fig. 22. COMSOL simulation for 1D topological metamaterial lattice when regular honeycomb hourglass metastructure k_h or hard-hard ($k_1 - k_1$) springs are attached adjacent to interface mass along with considered damping and excitation given at one end and response is taken at the interface. (a), (b) and (c) Frequency Response Function corresponding to damping $c = 0.0001, 0.001$ and 0.01 N-s/m respectively. (d), (e) and (f) Phase plot corresponding to damping $c = 0.0001, 0.001$ and 0.01 N-s/m respectively. The parameters considered are : $m = 1$ kg, $k = 1$ N/m, $k_1 = k(1 + \gamma), k_2 = k(1 - \gamma)$, $\gamma = 0.4$.

isolating, switching, filtering, and precision positioning [43]. The resulting localized non-trivial interface mode can also be used to design antifracture materials, vibration isolators, and on-chip transducers [21]. Applications like sensors, ultrasound imaging, and therapy may benefit from topological interface states. Surface acoustic wave devices might benefit from the robustness of topological modes, which is important for wave transfer applications.

4.4. Effect of damping on the topological metamaterial lattice

Finally, the effect of damping on the current topological metamaterial has been analyzed using simulations performed in COMSOL. Different values of damping coefficients have been taken into account such that $c = 0.0001, 0.001,$ and 0.01 N-s/m; $m = 1$ kg, $k = 1$ N/m, $\gamma = 0.4$, $\chi = 1$, $k_1 = k(1 + \gamma)$, and $k_2 = k (1 - \gamma)$, with identical masses m, in the configuration of the hard-hard ($k_1 - k_1$) and soft-soft ($k_2 - k_2$) spring mounted at the adjacent sides of the interface mass. The amplitude of the interface mode tends to diminish when damping is increased, and its presence is observable from the phase shift seen in the phase plot. Additionally, it was previously noted that in the absence of damping, the phase tended to shoot up, however, this is not the case in the presence of damping, since the edge of the phase diagram has a smooth curve. In the honeycomb hourglass metastructure, increasing the damping would lead to a decrease in the amplitude of the second interface mode, also above the optical branch. As shown in Figs. 22(a) to (f) and 23(a) to (f), the effect of damping on both lattices of a regular honeycomb and auxetic structure are investigated with frequency response function and phase plot, which indicates the distinct presence of interface mode. The magnitude of the interface modes in the COMSOL simulation for the modified lattice was not large possibly due to the lack of proper discretization of frequency range values in COMSOL. However, the experimental findings show high amplitude of the interface mode.

5. Conclusion

Our study primarily illustrates analytically and also through computational simulation and experimental studies that the tunable localized modes can be induced at the interface or boundaries of one-dimensional lattices by incorporating the novel hourglass lattice metastructure. Quantitative measurements for different configurations of springs at the adjacent side of the interface are presented to switch the position of a localized mode within the bandgap. The piezo-electric-based energy harvesting within the isolation zone (i.e., bandgap) at a specific frequency has been obtained successfully. The voltage magnitude and related frequency may be controlled by using an hourglass lattice oscillator by breaking the inversion symmetry in the periodic elastic structures. The significant findings from the study are as follows:
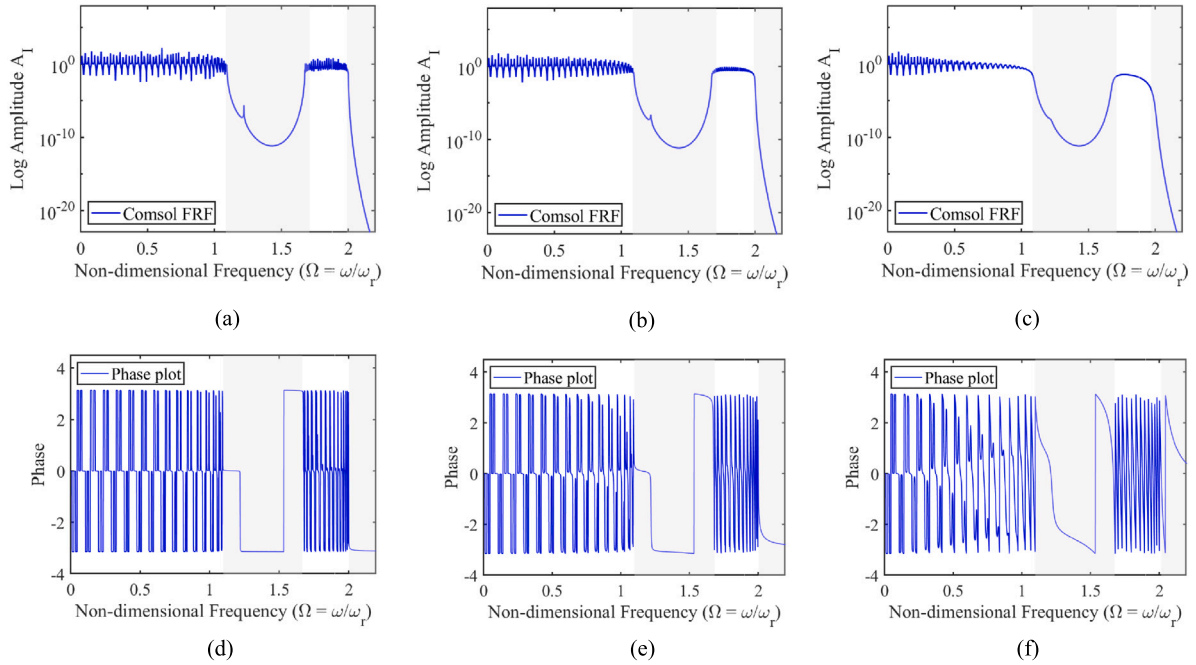
Fig. 23. COMSOL simulation for 1D topological metamaterial lattice when auxetic metastructure k_a or soft-soft $(k_2 - k_2)$ springs are attached adjacent to interface mass along with considered damping and excitation given at one end and response is taken at the interface. (a), (b) and (c) Frequency Response Function corresponding to damping $c = 0.0001, 0.001$ and 0.01 N-s/m respectively. (d), (e) and (f) Phase plot corresponding to damping $c = 0.0001, 0.001$ and 0.01 N-s/m respectively. The parameters considered are : $m = 1$ kg, $k = 1$ N/m, $k_1 = k(1 + \gamma)$, $k_2 = k(1 - \gamma)$, $\gamma = -0.4$.

- In the one-dimensional case, we consider a lattice of point masses connected by alternating springs. The interface mass can be strategically placed at the desired locations of the lattice where the localized mode is required to be obtained. The localized interface mode is achieved successfully by placing the mirror copies of the left and the right sublattice for the purpose of wave-guiding at a precise frequency and energy harvesting.
- We derived explicit expressions for the frequencies of the localized modes for various interface types and their associated mode shapes. We demonstrated how varying the cellular configuration of the additively manufactured hourglass could lead to a frequency shift of the interface mode. By choosing the geometrical parameters suitably one can control the location of interface modes and move them from the left to the right side of the bulk modes. For example, a hard-hard interface can place the mode at the centre of the bandgap, while a soft-soft interface can shift it to the left. Again, by using a generic hourglass structure at interface one can shift it to the right side of the bandgap.
- Moreover, piezo-electric-based energy harvesting is carried out using bimorph cantilever model. The power expressions are derived explicitly and subsequently found depending upon the hourglass lattice parameters, and we demonstrate the frequency-dependent power modulation experimentally. The amplitude-dependent peak voltages obtained under different conditions of spring stiffness at the interface positions are 12.59 mV (for soft-soft spring case) and 8.72 mV (for the generalized case), respectively. The peak power value for these cases turned out to be 0.062 μW and 0.03 μW respectively.
- Finally, the effect of damping has been analyzed, which shows that the amplitude of the interface mode tends to diminish with damping increments, and its presence is still noticeable from the phase shift seen in the phase plots.

This work can be further extended to evaluate amplitude-dependent frequency response at the interface by exploring the hourglass lattice-based nonlinearities that can lead to tunable topological lattices.

CRediT authorship contribution statement

Harsh Mirani: Conceptualization, Methodology, Investigation, Software, Writing – original draft. **Vivek Gupta:** Conceptualization, Methodology, Investigation, Software, Writing – original draft. **Sondipon Adhikari:** Conceptualization, Project administration, Writing – review & editing. **Bishakh Bhattacharya:** Conceptualization, Experiment ideation, Project administration, Writing – review & editing.

Declaration of competing interest

Data availability

Data will be made available on request.

Acknowledgments

The authors gratefully acknowledge the grants received from "Scheme for Promotion of Academic and Research Collaboration" (SPARC) and the Ministry of Human Resource Development, Govt. of India (MHRD) through grant number MHRD/ME/2018544 and also the support of UK-India Education and Research Initiative (UKIERI) through grant number UKIERI/P1212.

Appendix

A.1. Sublattice - B : Displacement relation

To obtain relation between two adjacent neighboring unit cells on right side of interface mass of modified topological metamaterial i.e. sublattice - B, the governing equations of motion for the masses of sub-lattice w_0 and v_1 may be written as

$$m\ddot{u}_{v,1} + k_1(u_{v,1} - u_{w,1}) + k_2(u_{v,1} - u_{w,0}) = 0 \tag{A.1.1}$$

$$m\ddot{u}_{w,0} + \chi k_1(u_{w,0} - u_{c,0}) + k_2(u_{w,0} - u_{v,1}) = 0 \tag{A.1.2}$$

Implementing the plane wave solution of the form $u_j = (u_{v,j}, u_{w,j}) = A(\mu)e^{i\mu j + i\Omega\tau}$ and substituting the values of stiffness in Eqs. (A.1.1) and (A.1.2) leads to

$$-\Omega^2 m u_{v,1} + k(1 + \gamma)(u_{v,1} - u_{w,1}) + k(1 - \gamma)(u_{v,1} - u_{w,1}) = 0 \tag{A.1.3}$$

$$-\Omega^2 m u_{w,0} + \chi k(1 + \gamma)(u_{w,0} - u_{c,0}) + k(1 - \gamma)(u_{w,0} - u_{v,1}) = 0 \tag{A.1.4}$$

The non-dimensional form of Eqs. (A.1.3) and (A.1.4) would result in

$$(2 - \Omega^2)u_{v,1} - (1 + \gamma)u_{w,1} - (1 - \gamma)u_{w,0} = 0 \tag{A.1.5}$$

$$(\chi + \chi\gamma + 1 - \gamma - \Omega^2)u_{w,0} - (1 - \gamma)u_{v,1} - \chi(1 + \gamma)u_{c,0} = 0 \tag{A.1.6}$$

$u_{v,1}$ can be expressed in terms of $u_{w,0}$ and $u_{c,0}$ as

$$u_{v,1} = \frac{\chi + \chi\gamma + 1 - \gamma - \Omega^2}{1 - \gamma}u_{w,0} + \frac{\chi(1 + \gamma)}{\gamma - 1}u_{c,0} \tag{A.1.7}$$

$$u_{v,1} = \frac{\chi(1 + \gamma)}{\gamma - 1}u_{c,0} + \frac{\chi + \chi\gamma + 1 - \gamma - \Omega^2}{1 - \gamma}u_{w,0} \tag{A.1.8}$$

Substituting $u_{v,1}$ from Eq. (A.1.8) in Eq. (A.1.5) and finding $u_{w,1}$ in terms of $u_{c,0}$ and $u_{w,0}$

$$(2 - \Omega^2)\chi\frac{(1 + \gamma)}{\gamma - 1}u_{c,0} + \frac{(2 - \Omega^2)(\chi + \chi\gamma + 1 - \gamma - \Omega^2)}{1 - \gamma}u_{w,0} - (1 + \gamma)u_{w,1} - (1 - \gamma)u_{w,0} = 0 \tag{A.1.9}$$

$$u_{w,1} = -\frac{2 - \Omega^2}{1 - \gamma}\chi u_{c,0} + \frac{(2 - \Omega^2)(\chi + \chi\gamma + 1 - \gamma - \Omega^2) - (1 - \gamma)^2}{1 - \gamma^2}u_{w,0} \tag{A.1.10}$$

Combining Eqs. (A.1.8) and (A.1.10) leads to

$$\begin{pmatrix} u_v \\ u_w \end{pmatrix}_1 = \begin{pmatrix} \dfrac{\chi(\gamma + 1)}{\gamma - 1} & \dfrac{(\chi + \chi\gamma + 1 - \gamma - \Omega^2)}{1 - \gamma} \\ -\dfrac{(2 - \Omega^2)\chi}{1 - \gamma} & \dfrac{(2 - \Omega^2)(\chi + \chi\gamma + 1 - \gamma - \Omega^2) - (1 - \gamma)^2}{1 - \gamma^2} \end{pmatrix} \begin{pmatrix} u_c \\ u_w \end{pmatrix}_0 = T_1 \begin{pmatrix} u_c \\ u_w \end{pmatrix}_0 \tag{A.1.11}$$

The relation of the unit cell adjacent to the interface mass unit cell is given by

$$\begin{pmatrix} u_v \\ u_w \end{pmatrix}_1 = T_1 \begin{pmatrix} u_c \\ u_w \end{pmatrix}_0 \tag{A.1.12}$$

The relationship between the unit cell next to the interface mass and the other unit cell advancing across the sublattice toward the free end of the lattice is given by the transfer matrix T previously computed in Eq. (31) as

$$\begin{pmatrix} u_v \\ u_w \end{pmatrix}_2 = T \begin{pmatrix} u_v \\ u_w \end{pmatrix}_1 \tag{A.1.13}$$

For the unit cell $N = 2$ and unit cell containing interface mass $N = 0$ is related by

$$\begin{pmatrix} u_v \\ u_w \end{pmatrix}_2 = TT_1 \begin{pmatrix} u_c \\ u_w \end{pmatrix}_0 \tag{A.1.14}$$

The displacement relation for the Nth unit cell on sublattice - B and the unit cell containing the localized interface mass can be obtained as

$$\begin{pmatrix} u_v \\ u_w \end{pmatrix}_N = T^{N-1} T_1 \begin{pmatrix} u_c \\ u_w \end{pmatrix}_0 \tag{A.1.15}$$

A.2. Sublattice - A : Displacement relation

The governing equations of motion for the masses w_{-1} and v_0 of the sublattice-A may be written as

$$m\ddot{u}_{w,-1} + k_2(u_{w,-1} - u_{v,-1}) + \chi k_1(u_{w,-1} - u_{c,0}) = 0 \tag{A.2.16}$$

$$m\ddot{u}_{c,0} + \chi k_1(2u_{c,0} - u_{w,-1} - u_{w,0}) = 0 \tag{A.2.17}$$

Implementing the plane wave solution of the form $u_j = (u_{v,j}, u_{w,j}) = A(\mu)e^{i\mu j + i\Omega \tau}$ and substituting values of stiffness in Eqs. (A.2.16) and (A.2.17) leads to

$$-\Omega^2 m u_{w,-1} + k(1 - \gamma)(u_{w,-1} - u_{v,-1}) + \chi k(1 + \gamma)(u_{w,-1} - u_{c,o}) = 0 \tag{A.2.18}$$

$$-\Omega^2 m u_{c,0} + \chi k(1 + \gamma)(2u_{c,0} - u_{w,-1} - u_{w,0}) = 0 \tag{A.2.19}$$

Non-dimensional form of Eqs. (A.2.18) and (A.2.19) would result in

$$(1 + \chi - \Omega^2)u_{w,-1} - \chi(1 + \gamma)u_{c,0} - (1 - \gamma)u_{v,-1} = 0 \tag{A.2.20}$$

$$(2\chi + 2\chi\gamma - \Omega^2)u_{c,0} - \chi(1 + \gamma)u_{w,-1} - \chi(1 + \gamma)u_{w,0} = 0 \tag{A.2.21}$$

Making $u_{w,-1}$ as subject from previous Eq. (A.2.21) and determining its expression in terms of $u_{w,0}$ and $u_{c,0}$ as

$$u_{w,-1} = \frac{(2\chi + 2\chi\gamma - \Omega^2)}{\chi(1 + \gamma)}u_{c,0} - u_{w,0} \tag{A.2.22}$$

Put $u_{w,-1}$ from Eq. (A.2.22) into Eq. (A.2.20) and finding $u_{v,-1}$ in terms of $u_{c,0}$ and $u_{w,0}$

$$(1 + \chi - \Omega^2)u_{w,-1} - \chi(1 + \gamma)u_{c,o} - (1 - \gamma)u_{v,-1} = 0 \tag{A.2.23}$$

$$\frac{(1 + \chi - \Omega^2)(2\chi + 2\chi\gamma - \Omega^2)}{\chi(1 + \gamma)}u_{c,0} - (1 + \chi - \Omega^2)u_{w,0} - \chi(1 + \gamma)u_{c,0} - (1 - \gamma)u_{v,-1} = 0 \tag{A.2.24}$$

$$u_{v,-1} = \frac{(((1 + \chi - \Omega^2)(2\chi + 2\chi\gamma - \Omega^2)) - (\chi^2(1 + \gamma)^2))}{\chi(1 + \gamma)(1 - \gamma)}u_{c,0} - \frac{(1 + \chi - \Omega^2)}{1 - \gamma}u_{w,0} \tag{A.2.25}$$

Combining Eqs. (A.2.22) and (A.2.25) leads to

$$\begin{pmatrix} u_v \\ u_w \end{pmatrix}_{-1} = \begin{pmatrix} \dfrac{(1 + \chi - \Omega^2)(2\chi + 2\chi\gamma - \Omega^2) - \chi^2(1 + \gamma)^2}{\chi(1 + \gamma)(1 - \gamma)} & -\dfrac{(1 + \chi - \Omega^2)}{1 - \gamma} \\[3mm] -\dfrac{(2\chi + 2\chi\gamma - \Omega^2)}{\chi(1 + \gamma)} & -1 \end{pmatrix} \begin{pmatrix} u_c \\ u_w \end{pmatrix}_0 = T_2 \begin{pmatrix} u_c \\ u_w \end{pmatrix}_0 \tag{A.2.26}$$

The relation of the unit cell adjacent to the interface mass unit cell is given by

$$\begin{pmatrix} u_v \\ u_w \end{pmatrix}_{-1} = T_2 \begin{pmatrix} u_c \\ u_w \end{pmatrix}_0 \tag{A.2.27}$$

While the transfer matrix T previously computed in Eq. (31) relates the relationship between the unit cell next to the interface mass and the other unit cell traveling along the sublattice towards the free end of the lattice

$$\begin{pmatrix} u_v \\ u_w \end{pmatrix}_{-2} = T \begin{pmatrix} u_v \\ u_w \end{pmatrix}_{-1} \tag{A.2.28}$$

For the unit cell $N = 2$ and the unit cell containing interface mass $N = 0$ are related by

$$\begin{pmatrix} u_v \\ u_w \end{pmatrix}_{-2} = TT_2 \begin{pmatrix} u_c \\ u_w \end{pmatrix}_0 \tag{A.2.29}$$

Similarly, we can get the displacement relation for the Nth unit cell on the sublattice - A and the unit cell containing the localized interface mass as

$$\begin{pmatrix} u_v \\ u_w \end{pmatrix}_{-N} = T^{N-1} T_2 \begin{pmatrix} u_c \\ u_w \end{pmatrix}_0 \tag{A.2.30}$$

To determine the relationship between stiffness parameter γ and non-dimensional frequency Ω for different values of χ, i.e. $\chi = 0.7, 1, 2, 10, 100...$, when a certain number of unit cells with altered interface stiffness are used in the numerical analysis, the eigenvalue problem of topological lattice formulated using Eq. (49) for interface mass is resolved.

References

[1] B. Wood, J. Pendry, Metamaterials at zero frequency, J. Phys.: Condens. Matter 19 (7) (2007) 076208.
[2] H. Ammari, B. Davies, E.O. Hiltunen, S. Yu, Topologically protected edge modes in one-dimensional chains of subwavelength resonators, J. Math. Pures Appl. 144 (2020) 17–49.
[3] C. Brendel, V. Peano, O. Painter, F. Marquardt, Snowflake phononic topological insulator at the nanoscale, Phys. Rev. B 97 (2) (2018) 020102.
[4] G. Ma, M. Xiao, C.T. Chan, Topological phases in acoustic and mechanical systems, Nat. Rev. Phys. 1 (4) (2019) 281–294.
[5] S. Zheng, G. Duan, B. Xia, Progress in topological mechanics, Appl. Sci. 12 (4) (2022) 1987.
[6] A.B. Khanikaev, S. Hossein Mousavi, W.-K. Tse, M. Kargarian, A.H. MacDonald, G. Shvets, Photonic topological insulators, Nature Mater. 12 (3) (2013) 233–239.
[7] S.H. Mousavi, A.B. Khanikaev, Z. Wang, Topologically protected elastic waves in phononic metamaterials, Nature Commun. 6 (1) (2015) 1–7.
[8] V. Peano, C. Brendel, M. Schmidt, F. Marquardt, Topological phases of sound and light, Phys. Rev. X 5 (3) (2015) 031011.
[9] X. Tan, B. Wang, S. Zhu, S. Chen, K. Yao, P. Xu, L. Wu, Y. Sun, Novel multidirectional negative stiffness mechanical metamaterials, Smart Mater. Struct. 29 (1) (2019) 015037.
[10] M.I. Hussein, M.J. Leamy, M. Ruzzene, Dynamics of phononic materials and structures: Historical origins, recent progress, and future outlook, Appl. Mech. Rev. 66 (4) (2014).
[11] Z. Chen, W. Zhou, C. Lim, Tunable frequency response of topologically protected interface modes for membrane-type metamaterials via voltage control, J. Sound Vib. 494 (2021) 115870.
[12] A. Stein, M. Nouh, T. Singh, Widening, transition and coalescence of local resonance band gaps in multi-resonator acoustic metamaterials: From unit cells to finite chains, J. Sound Vib. 523 (2022) 116716.
[13] S. Yang, J.H. Page, Z. Liu, M.L. Cowan, C.T. Chan, P. Sheng, Focusing of sound in a 3D phononic crystal, Phys. Rev. Lett. 93 (2) (2004) 024301.
[14] A.N. Norris, Acoustic cloaking theory, Proc. R. Soc. A 464 (2097) (2008) 2411–2434.
[15] L. Ai, X.-L. Gao, Metamaterials with negative Poisson's ratio and non-positive thermal expansion, Compos. Struct. 162 (2017) 70–84.
[16] J.B. Pendry, Negative refraction makes a perfect lens, Phys. Rev. Lett. 85 (18) (2000) 3966.
[17] C. Goffaux, J. Vigneron, Theoretical study of a tunable phononic band gap system, Phys. Rev. B 64 (7) (2001) 075118.
[18] R.K. Pal, J. Vila, M. Leamy, M. Ruzzene, Amplitude-dependent topological edge states in nonlinear phononic lattices, Phys. Rev. E 97 (3) (2018) 032209.
[19] D. Qi, Z. Ren, Z. Qu, Valley-protected topological interface state of the elastic wave: From discrete model to multistable mechanical metamaterials, J. Sound Vib. 529 (2022) 116908.
[20] L. D'Alessandro, A.O. Krushynska, R. Ardito, N.M. Pugno, A. Corigliano, A design strategy to match the band gap of periodic and aperiodic metamaterials, Sci. Rep. 10 (1) (2020) 1–13.
[21] H. Huang, J. Chen, S. Huo, Recent advances in topological elastic metamaterials, J. Phys.: Condens. Matter 33 (50) (2021) 503002.
[22] M.I. Rosa, R.K. Pal, J.R. Arruda, M. Ruzzene, Edge states and topological pumping in spatially modulated elastic lattices, Phys. Rev. Lett. 123 (3) (2019) 034301.
[23] Y. Liu, L. Jin, H. Wang, D. Liu, Y. Liang, Topological interface states in translational metamaterials for sub-wavelength in-plane waves, Int. J. Mech. Sci. 197 (2021) 106308.
[24] M. Moscatelli, R. Ardito, L. Driemeier, C. Comi, Band-gap structure in two-and three-dimensional cellular locally resonant materials, J. Sound Vib. 454 (2019) 73–84.
[25] R.K. Pal, J. Vila, M. Ruzzene, Topologically protected edge states in mechanical metamaterials, Adv. Appl. Mech. 52 (2019) 147–181.
[26] H. Mirani, V. Gupta, S. Adhikari, B. Bhattacharya, Interface modes in topologically protected edge states using hourglass based metastructures, in: Active and Passive Smart Structures and Integrated Systems XVI, Vol. 12043, SPIE, 2022, pp. 473–480.
[27] M. Cajić, D. Karličić, J. Christensen, S. Adhikari, Tunable topological interface states in one-dimensional inerter-based locally resonant lattices with damping, J. Sound Vib. 542 (2023) 117326.
[28] Y. Li, Y. Luo, X. Zhang, Topological design of phononic crystals for multiple wide band gaps, J. Sound Vib. 529 (2022) 116962.
[29] V. Gupta, R.K. Munian, B. Bhattacharya, Dispersion analysis of the hourglass-shaped periodic shell lattice structure, Int. J. Solids Struct. (2022) 111931.
[30] V. Gupta, S. Adhikari, B. Bhattacharya, Exploring the dynamics of hourglass shaped lattice metastructures, Sci. Rep. 10 (1) (2020) 1–12.
[31] V. Gupta, B. Bhattacharya, S. Adhikari, Energy absorption of hourglass shaped lattice metastructures, Exp. Mech. (2022) 1–10.
[32] N. Easey, D. Chuprynyuk, W.S.W. Musa, A. Bangs, Y. Dobah, A. Shterenlikht, F. Scarpa, Dome-shape auxetic cellular metamaterials: manufacturing, modeling, and testing, Front. Mater. 6 (2019) 86.
[33] N. Novak, M. Vesenjak, Z. Ren, Auxetic cellular materials-a review, StrojniŠKi Vestnik-J. Mech. Eng. 62 (9) (2016) 485–493.
[34] K.K. Saxena, R. Das, E.P. Calius, Three decades of auxetics research- materials with negative Poisson's ratio: a review, Adv. Eng. Mater. 18 (11) (2016) 1847–1870.
[35] A. Alderson, K. Alderson, Auxetic materials, Proc. Inst. Mech. Eng. G 221 (4) (2007) 565–575.
[36] F. Farzbod, M.J. Leamy, The treatment of forces in Bloch analysis, J. Sound Vib. 325 (3) (2009) 545–551.
[37] M.I. Hussein, I. Patrick, A. Banerjee, S. Adhikari, Metadamping in inertially amplified metamaterials: Trade-off between spatial attenuation and temporal attenuation, J. Sound Vib. 531 (2022) 116977.
[38] Z. Chen, G. Wang, F. Shi, C. Lim, Analytical modeling and numerical analysis for tunable topological phase transition of flexural waves in active sandwiched phononic beam systems, Int. J. Mech. Sci. 223 (2022) 107292.
[39] Y. Chen, B. Wu, J. Li, S. Rudykh, W. Chen, Low-frequency tunable topological interface states in soft phononic crystal cylinders, Int. J. Mech. Sci. 191 (2021) 106098.
[40] J. Yin, M. Ruzzene, J. Wen, D. Yu, L. Cai, L. Yue, Band transition and topological interface modes in 1D elastic phononic crystals, Sci. Rep. 8 (1) (2018) 1–10.
[41] W. Zhou, C. Lim, et al., Topological edge modeling and localization of protected interface modes in 1D phononic crystals for longitudinal and bending elastic waves, Int. J. Mech. Sci. 159 (2019) 359–372.
[42] K. Bertoldi, V. Vitelli, J. Christensen, M. Van Hecke, Flexible mechanical metamaterials, Nat. Rev. Mater. 2 (11) (2017) 1–11.

[43] L. Xin, Y. Siyuan, L. Harry, L. Minghui, C. Yanfeng, Topological mechanical metamaterials: A brief review, Curr. Opin. Solid State Mater. Sci. 24 (5) (2020) 100853.

[44] Z. Zheng, J. Yin, J. Wen, D. Yu, Multiple topological interface states in broadband locally resonant phononic crystals, J. Appl. Phys. 129 (18) (2021) 184901.

[45] P. Wang, L. Lu, K. Bertoldi, Topological phononic crystals with one-way elastic edge waves, Phys. Rev. Lett. 115 (10) (2015) 104302.

[46] A. Erturk, D.J. Inman, A distributed parameter electromechanical model for cantilevered piezoelectric energy harvesters, J. Vib. Acoust. 130 (4) (2008).

[47] M.A. Hasan, L. Calderin, P. Lucas, K. Runge, P.A. Deymier, Geometric phase invariance in spatiotemporal modulated elastic system, J. Sound Vib. 459 (2019) 114843.

[48] M. Xiao, G. Ma, Z. Yang, P. Sheng, Z. Zhang, C.T. Chan, Geometric phase and band inversion in periodic acoustic systems, Nat. Phys. 11 (3) (2015) 240–244.

[49] C.-S. Lee, I.-F. Io, H.-c. Kao, Winding number and Zak phase in multi-band SSH models, Chinese J. Phys. 78 (2022) 96–110.

[50] X. Li, Y. Meng, X. Wu, S. Yan, Y. Huang, S. Wang, W. Wen, Su-Schrieffer-Heeger model inspired acoustic interface states and edge states, Appl. Phys. Lett. 113 (20) (2018) 203501.

[51] A. Erturk, D.J. Inman, An experimentally validated bimorph cantilever model for piezoelectric energy harvesting from base excitations, Smart Mater. Struct. 18 (2) (2009) 025009.

[52] A. Erturk, D.J. Inman, Issues in mathematical modeling of piezoelectric energy harvesters, Smart Mater. Struct. 17 (6) (2008) 065016.

[53] F. Lucklum, M.J. Vellekoop, Bandgap engineering of three-dimensional phononic crystals in a simple cubic lattice, Appl. Phys. Lett. 113 (20) (2018) 201902.